

2020-02

Aerodynamic Analysis of a Two-Bladed Vertical-Axis Wind Turbine Using a Coupled Unsteady RANS and Actuator Line Model

Zhao, R

<http://hdl.handle.net/10026.1/17673>

10.3390/en13040776

Energies

MDPI AG

All content in PEARL is protected by copyright law. Author manuscripts are made available in accordance with publisher policies. Please cite only the published version using the details provided on the item record or document. In the absence of an open licence (e.g. Creative Commons), permissions for further reuse of content should be sought from the publisher or author.

1 Article

2 Aerodynamic Analysis of a Two-Bladed Vertical-Axis 3 Wind Turbine Using a Coupled Unsteady RANS and 4 Actuator Line Model

5 Ruiwen Zhao ^{1,*}, Angus C. W. Creech ¹, Alistair G. L. Borthwick ¹, Vengatesan Venugopal ¹ and
6 Takafumi Nishino ²

7 ¹ Institute for Energy Systems, School of Engineering, The University of Edinburgh, King's Buildings,
8 Edinburgh EH9 3BF, Scotland, UK; a.creech@ed.ac.uk (A.C.W.C); alistair.borthwick@ed.ac.uk (A.G.L.B);
9 v.venugopal@ed.ac.uk (V.V)

10 ² Department of Engineering Science, University of Oxford, Parks Road, Oxford OX1 3PJ, England, UK;
11 takafumi.nishino@eng.ox.ac.uk (T.N)

12 * Correspondence: r.zhao@ed.ac.uk;

13 Received: 4 November 2019; Accepted: 8 February 2020; Published: date

14 **Abstract:** Close-packed contra-rotating vertical-axis turbines have potential advantages in wind and
15 hydrokinetic power generation. This paper describes the development of a numerical model of a
16 vertical axis turbine with a torque-controlled system using an actuator line model (ALM). The
17 developed model, coupled with the open-source OpenFOAM computational fluid dynamics (CFD)
18 code, is used to examine the characteristics of turbulent flow behind a single two-bladed vertical-
19 axis turbine (VAT). The flow field containing the turbine is simulated by solving the unsteady
20 Reynolds-averaged Navier-Stokes (URANS) equations with a $k-\omega$ shear stress transport (SST)
21 turbulence model. The numerical model is validated against experimental measurements from a
22 two-bladed H-type wind turbine. Turbine loading is predicted, and the vorticity distribution is
23 investigated in the vicinity of the turbine. Satisfactory overall agreement is obtained between
24 numerical predictions and measured data on thrust coefficients. The model captures important
25 three-dimensional flow features that contribute to wake recovery behind a vertical-axis turbine,
26 which will be useful for future studies of close-packed rotors with a large number of blades.

27 **Keywords:** vertical-axis turbine; actuator line method; torque control; URANS; OpenFOAM; wind
28 energy
29

30 1. Introduction

31 Climate change mitigation is vitally important for all nations in the world, given that
32 greenhouse-gas (GHG) emissions have increased by over one-quarter since 1995 [1], as reported at
33 the first United Nations (UN) Conference of the Parties (COP). Moreover, energy consumption by
34 developed and developing countries has been projected to increase by 28% from 2015 to 2040 [2]. A
35 key approach to replacing fossil fuels as an energy source and limiting carbon release is to invest in
36 renewable energy technology [3]. Wind and hydrokinetic energy are particularly attractive options
37 for sustainable electricity generation from low-carbon sources [4], and are likely to become significant
38 contributors to the electricity supply by 2030 [1]. Much ongoing research into the development of
39 wind and tidal turbines focuses on horizontal- and vertical-axis turbines [5]. Salter [6] compared
40 vertical-axis transverse-flow turbines with horizontal-axis axial-flow turbines in terms of flow
41 impedance, turbulence, blockage ratio, installation, pitch change, and navigation, with tidal flow in
42 the Pentland Firth, Scotland, in mind. Salter found that high blockage (or sweepage), vertical-axis,
43 variable-pitch rotors could lead to substantially higher potential power generation for high
44 impedance flows [6]. Such vertical-axis transverse-flow tidal turbines tolerate uneven seabed

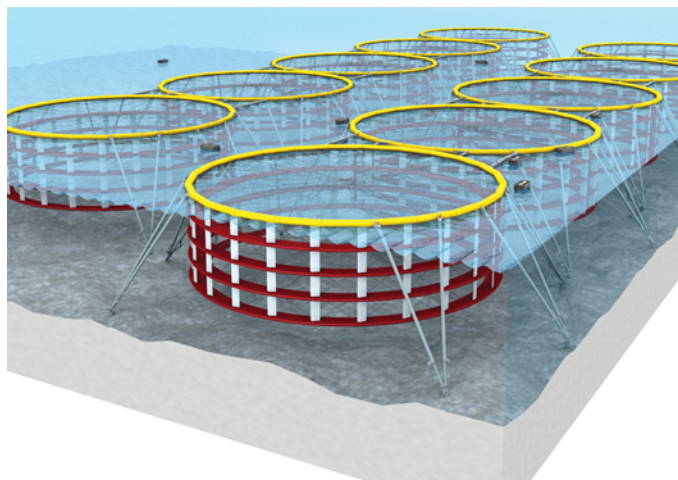
45 topography and may attain an even pressure drop by controlling the blade pitch, hence reducing
46 wake turbulence [6]. Vertical-axis turbines thus appear to offer a promising near-term technology for
47 tidal energy. Initial study of vertical-axis turbine (VAT) technology began in the 1970s at Sandia
48 National Laboratories where researchers investigated vertical-axis turbine configurations, including
49 Savonius (torque generated from drag) and Darrieus (torque generated from lift) turbines [7,8]. The
50 Savonius turbine can accept flow from any direction and is self-starting, with low cut-in speed;
51 however, the Savonius turbine is restricted to fewer applications due to its inefficiency at relatively
52 low tip speed ratios [9]. Darrieus turbines have higher cut-in speed than equivalent Savonius turbines,
53 and so rotate faster than the inflow velocity, attaining higher coefficients of performance [9,10], even
54 though their support arms introduce additional aerodynamic drag [11]. To solve this problem, Salter
55 and Taylor [12] proposed the innovative vertical-axis rotor system shown in Figure 1. Computational
56 fluid dynamics (CFD) has been widely used in the systematic analyses of vertical-axis turbines [13–
57 29]. Actuator-type models parameterize the turbine loading and thus reduce computational expense,
58 but do not resolve the fine detail of the blade boundary layers [30]. Four approaches have commonly
59 been used to represent turbines in such models, namely: actuator disc with rotation or blade element
60 momentum (BEM) [31–35]; actuator disk without rotation [30,35,36]; actuator surface [37–39]; and
61 actuator line [30,40,41]. BEM is an analytical method, whereas the actuator disc with rotation model
62 is a combination of blade-element (BE) theory and CFD, which solves the Navier-Stokes equations to
63 satisfy the momentum balance [35]. The actuator disc with rotation model is computationally efficient,
64 but does not directly include the influence of vortices shed from blade tips on the induced velocity
65 [31]. The uniform actuator disk without rotation model is limited in applicability because of its
66 simplifying assumptions [37], and has proved unsatisfactory as a wake generator method for a cross-
67 flow turbine [40]. The actuator surface technique accurately predicts the flow structure near blades
68 and in the tip vortex region, but requires a fine mesh passing smoothly over the airfoil surface [38].
69 The actuator line model (ALM) [42,43] is better at capturing three-dimensional (3D) vortical
70 structures in the near wake than actuator disc approaches [44], and so is used herein. ALM has been
71 used to model vertical-axis turbines at low Reynolds number based on rotor diameter $Re_D \sim 10^4$, and
72 of large and medium solidity (chord-to-radius ratio) at high Re_D around 10^6 [30,45].

73 In order to simulate the wake dynamics properly, a suitable turbulence closure model is required
74 within the CFD codes. Typically, $k-\varepsilon$ Reynolds-averaged Navier-Stokes (RANS) [46–48], $k-\omega$
75 RANS [46,48,49], and large eddy simulation (LES) [50,51] models have been used for CFD simulations
76 of flows interacting with horizontal-axis turbines [52–56] and vertical-axis turbines [13,16–18,20–
77 23,25,26]. Although RANS approaches are relatively inexpensive, they have the drawback that they
78 are unable accurately to predict all types of turbulent flow [46]. LES [50,51] resolves turbulence in a
79 partly statistical, partly explicit manner, and reduces computational cost through low-pass filtering.
80 Even so, LES is substantially more expensive computationally than RANS, which is why it is used
81 rather sparingly in simulations of turbulent flow past horizontal-axis turbines and vertical-axis
82 turbines.

83 Typical recent applications of CFD to turbines follow. McLaren [57] reported a numerical and
84 experimental study of the unsteady loading on a small-scale, high-solidity, H-type Darrieus turbine,
85 based on two-dimensional (2D), unsteady Reynolds-averaged Navier-Stokes (URANS) simulations
86 by CFD ANSYS-CFX. The study revealed the dominant effect of dynamic stall on the output power
87 and vibration excitation of the turbine. Nobile et al. [58] later simulated 2D unsteady-flow past a
88 Giromill wind turbine, also using ANSYS-CFX, finding that mesh resolution and choice of turbulence
89 model had a substantial effect on accuracy, with time step having only a slight impact on the
90 numerical results. Biadgo et al. [59] used a stream-tube approach to undertake a numerical and
91 analytical assessment of the performance of a vertical-axis wind turbine comprising a straight-bladed
92 fixed-pitch Darrieus turbine with a NACA 0012 blade profile using ANSYS FLUENT. These
93 numerical predictions were compared with analytical results obtained using a double multiple
94 streamtube (DMST) model, which exhibited inability using both CFD and DMST for the turbine to
95 be self-starting owing to minimum and/or negative torque and performance at very low tip-speed
96 ratios. Bachant et al. [60] developed a validated ALM of a vertical-axis turbine with both high and

97 medium values of solidity, and tested both $k-\varepsilon$ RANS and Smagorinsky LES turbulence models in
98 the OpenFOAM CFD framework. Bachant et al. found that RANS models running on coarse grids
99 were able to provide good convergence behaviour in terms of the mean power coefficient. Compared
100 with other 3D blade-resolved RANS simulations [60,61], Bachant et al.'s model achieved
101 approximately four orders of magnitude reduction in computational expense by implementing
102 corrections in sub-models for the effects of dynamic stall, end conditions, added mass, and flow
103 curvature. Given that such models have focused on idealized vertical-axis turbines, further
104 investigation into optimal practical models with fewer correction factors is still required.

105 Figure 1 shows a group of close-packed contra-rotating vertical-axis rotors, designed by Stephen
106 Salter to maximise the fraction of flow passage swept [12]. Blockage is estimated to increase to 80%
107 given the small gaps between the rotors, which are controlled by a hydraulic ram. The rotor diameter
108 should be at least three times the water depth in order to provide stability in pitch and roll of a single
109 rotor, and this should be doubled for a close-packed array. This contributes to a high blockage
110 fraction allowing generation well above the Betz limit for rotors in channels [6]. Following Buntine
111 and Pullin [62], the design concept is based on two vortices of opposite-sign cancelling each other out,
112 and thus conditioning the flow through the turbine while lowering the turbulence kinetic energy in
113 the wake. The turbine downstream area will then experience less stream-wise flow variation,
114 reducing mixing loss and therefore enhancing energy extraction. To predict the commercial feasibility
115 of this large-scale marine hydrokinetic application, a numerical model of such devices is required.



116 **Figure 1.** Artist's impression of close-packed vertical-axis contra-rotating rotors [12].

117 This paper describes a numerical model of a cross-flow turbine, with the future goal of modelling
118 close-packed tidal rotors comprising many blades. The present model is built upon a previous turbine
119 model, which scales to thousands of cores on a supercomputer [54,56]. Although the present focus is
120 on a single rotor, the numerical model can be applied to a large-scale turbine farm in future studies.
121 Due to a lack of experimental data concerning this type of rotor, the numerical model is first validated
122 against experimental measurements from a two-bladed H-type wind turbine, and then used to
123 predict turbine loading and investigate vorticity distribution in the vicinity of the rotor.

124 A newly developed, efficient, parallelised, numerical model of vertical-axis turbines, with a fixed
125 tip-speed ratio system and with a torque-controlled system, is presented in the following sections.
126 This computationally efficient numerical model is coupled with and is developed within the
127 OpenFOAM CFD framework. Unique features of the present model include torque control and active
128 pitch mechanisms. For brevity, only the torque-controlled system is presented in this paper; pitch
129 control mechanisms for solving the dynamic stall problem as well as performance optimization [63,64]
130 will be explored in future work. We believe that the application of the present model to a torque-
131 controlled vertical-axis turbine gives new insight into the aerodynamic behaviour of vertical-axis
132 wind turbines, in particular the difference in behaviour between an idealised turbine with fixed tip-
133 speed ratio and a more practical turbine with torque control.

134 2. Mathematical Model

135 Flow past a single vertical-axis turbine (VAT) with an arbitrary number of blades is simulated
 136 using an adapted version of the Wind and Tidal Turbine Embedded Simulator (WATTES), which is
 137 an efficient, parallelised, two-way coupled turbine model of horizontal-axis turbines, scaling to
 138 thousands of computing cores [54,56]. We denote the newly developed model WATTES-V. A
 139 preparatory set-up of the original WATTES model using the OpenFOAM CFD solver was conducted
 140 to ensure the codes were correctly coupled [65]; details of the software architecture are provided in
 141 Appendix A. This prerequisite ensures that WATTES-V model benefits from the advantages of the
 142 original model. One unique feature of the modified WATTES-V model is that it enables torque control;
 143 the main benefit of torque-controlled models is their prediction of the dynamic response of the
 144 turbine to the flow [52–54]. The mathematical formulation of WATTES-V is provided below.

145 2.1. Frame of Reference

146 To calculate the body forces, the coordinates of nodes in the mesh are first translated to the frame
 147 of reference of the rotor, in a similar manner to the original WATTES model [54]. The centre of the
 148 vertical-axis turbine is located at position O (see Figure 2), where $\vec{x}_O = (x_O, y_O, z_O)$. The azimuthal
 149 angle, which describes the orbital path taken by the first turbine blade, is denoted θ . In WATTES-V,
 150 θ starts from the x -axis, as indicated in Figure 2. The coordinates of a blade reference frame are
 151 denoted x', y', z' , with $O'(x', y', z')$ the origin of the new reference system. In the blade reference
 152 frame, the coordinates of a transformed point at position $\vec{x}' = (x', y', z')$ are:

$$\vec{x}' = (x', y', z') = R(\theta) \begin{bmatrix} x - x_O \\ y - y_O \\ z - z_O \end{bmatrix}, \quad (1)$$

153 where

$$R(\theta) = \begin{bmatrix} \cos \theta & \sin \theta & 0 \\ -\sin \theta & \cos \theta & 0 \\ 0 & 0 & 1 \end{bmatrix}. \quad (2)$$

154 Similarly, the localised velocity at a given point is $\vec{u} = (u, v, w)$, and this is transformed to the
 155 rotor's frame of reference as $\vec{u}' = R(\theta)\vec{u}$. Once in this frame of reference, the model calculates the
 156 momentum source terms, and then a second transformation takes place before passing these back to
 157 the CFD solver (cf. Creech et al [54]). To simplify the notation, we denote the transformed coordinates
 158 and velocity as \vec{x} and \vec{u} hereafter.

159 2.2. Lift and Drag Calculations

160 The actuator line method (ALM) [43] creates a distribution of body forces along a set of line
 161 segments representing the blades of a turbine. For each turbine rotor, only grid points found within
 162 the hollow cylindrical volume V traced out by the rotating blades are considered.

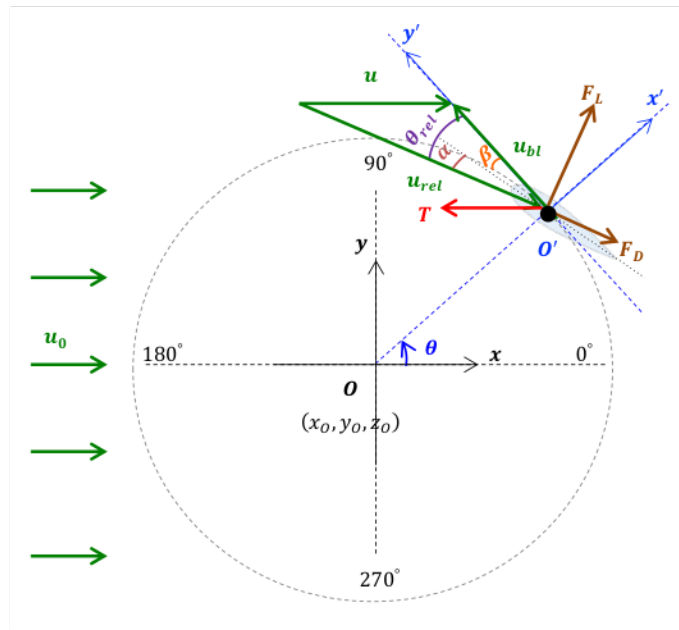
163 The lift and drag force vectors per unit span on a blade are given by:

$$\vec{f}_L = \frac{\text{lift}}{\text{unit span}} = \frac{1}{2} \rho C_L(\alpha, Re) |\vec{u}_{rel}|^2 c(z) \vec{e}_L, \quad (3)$$

$$\vec{f}_D = \frac{\text{drag}}{\text{unit span}} = \frac{1}{2} \rho C_D(\alpha, Re) |\vec{u}_{rel}|^2 c(z) \vec{e}_D, \quad (4)$$

164 where ρ is the fluid density, and C_L and C_D are the lift and drag coefficients, which depend on the
 165 angle of attack α and the Reynolds number Re of the flow over the blade. The magnitude of relative
 166 velocity of the fluid over the blade is $|\vec{u}_{rel}|$, and $c(z)$ is the blade chord length, which can vary along
 167 the blade span, but in the present case is constant. As the blades are parallel to z -axis, this is a function
 168 of z . The unit vectors \vec{e}_L and \vec{e}_D are in the direction of lift and drag respectively. Values of C_L and
 169 C_D are given in tabulated form [54], and as with most models, these are derived from an assumption
 170 of two-dimensional flow over the blade. Figure 2 shows a schematic diagram illustrating a turbine
 171 blade with chord, pitch, and path of a single blade. The diagram also indicates the force component

172 vectors that provide loading on the blade. The black dashed circle represents the circular trajectory
 173 of a blade.



174 **Figure 2.** Geometry of and force vectors on a blade of a rotating vertical-axis turbine (VAT). The flow
 175 velocity relative to the blades is \vec{u}_{rel} ; the angle of attack α is calculated from the local inflow velocity
 176 \vec{u} ; the freestream velocity \vec{u}_0 ; and the blade velocity is \vec{u}_{bl} . The azimuthal blade angle is θ with the
 177 corrected blade pitch β ; and θ_{rel} is relative angle. F_L and F_D are lift and drag forces per unit span
 178 respectively for the actuator line.

179 The relative velocity \vec{u}_{rel} is calculated for each point within the control volume V at a radial
 180 distance r from the rotor center (along z -axis) as

$$\vec{u}_{rel} = \vec{u} - \vec{u}_{bl}, \quad (5)$$

181 where \vec{u}_{bl} is the blade velocity. For a vertical-axis turbine, the magnitude of \vec{u}_{rel} is

$$u_{rel} = |\vec{u}_{rel}| = \sqrt{u^2 + v^2 + u_{bl}^2 + 2 u_{az} u_{bl}}, \quad (6)$$

182 where $u_{bl} = r\omega_{bl}$, and ω_{bl} is the angular velocity of blade. Note that the spanwise velocity
 183 component is neglected here, because the spanwise component of flow velocity is assumed to have
 184 minimal impact on the performance of the blade, and so tip-loss effects can be ignored. The azimuthal
 185 component of the fluid velocity is given as

$$u_{az} = -\frac{1}{r} (x v - y u). \quad (7)$$

186 This is necessary to account for the rotation of the flow, as lift and drag forces act to turn the
 187 blades and the generator, resulting in an equal and opposite reaction force acting on the flow, causing
 188 it to rotate in the opposite direction to that of the blades [54].

189 The flow angle relative to that of the fluid is

$$\theta_{rel} = \tan^{-1} \left(\frac{u \cos \theta + v \sin \theta}{-u \sin \theta + v \cos \theta - \omega_{bl} r} \right). \quad (8)$$

190 The local angle of attack is then computed from θ_{rel} as follows:

$$\alpha = \theta_{rel} - \beta, \quad (9)$$

191 where the local blade angle β is given by

$$\beta = \beta_p + \beta_t. \quad (10)$$

192 The blade pitch angle β_p can be actively controlled, as with [54], but for the present validation
 193 work it is kept constant at $\beta_p = 0$. The local blade twist angle β_t is calculated from the blade
 194 geometry but we consider straight blades and hence $\beta_t = 0$ in the present test cases.

195 Lift and drag forces per unit span are then calculated using the WATTES-V actuator line
 196 representation of each blade, which utilises a two-dimensional Gaussian regularization kernel $\eta_i(d_i)$
 197 [56]:

$$\begin{aligned}\vec{F}_L &= \sum_{i=1}^{N_{bl}} \eta_i(d_i) \vec{f}_{L_i}, \\ \vec{F}_D &= \sum_{i=1}^{N_{bl}} \eta_i(d_i) \vec{f}_{D_i},\end{aligned}\quad (11)$$

198 where N_{bl} is the number of blades, d_i is the shortest distance between a given point and the i^{th}
 199 actuator line. The pointwise lift and drag per unit span, \vec{f}_{L_i} and \vec{f}_{D_i} , are obtained from Equations (3)
 200 and (4). A two-dimensional Gaussian regularization kernel operates in the blade azimuthal direction
 201 and smears the solution in a circle [56], such that:

$$\eta_i(d_i) = \frac{1}{2\pi\sigma^2} e^{-\frac{d_i^2}{2\sigma^2}}, \quad (12)$$

202 where the distance from the i^{th} vertical actuator line is $d_i = \sqrt{(x - x_i)^2 + (y - y_i)^2}$, with x_i and y_i
 203 the local coordinates of blade i , x and y are the point coordinates, and the standard deviation σ
 204 determines the width of the Gaussian kernel.

205 The value of σ was chosen carefully so that it is neither too large (smeared solution) nor too
 206 small (extremely high resolution, and correspondingly small time step) [56]. Experiments determined
 207 that numerical stability was optimal when the Gaussian width was set to twice the local cell length,
 208 Δx , as also by Troldborg [30,43]. Other researchers have investigated the effect of the standard
 209 deviation (or projection width) on accuracy and stability: Schito and Zasso [30,66] found that the
 210 equivalent of the mesh cell width was ideal; Jha et al. [30,67] recommended using an equivalent
 211 elliptic planform for its calculation; Martinez-Tossas and Meneveau [30,68] used two-dimensional
 212 potential flow analysis to determine the optimal projection width; Tennekes and Lumley [69]
 213 recommended the projection width to be of the order of the momentum thickness θ_{mt} [30]. Here, the
 214 Gaussian width related to mesh size is estimated as $\Delta x \approx \sqrt[3]{V_{cell}}$ where V_{cell} is the cell volume.
 215 Following Bachant et al. [30], an additional factor $C_{mesh} = 2.0$ is introduced, and non-unity aspect
 216 ratio cells incorporated using $\sigma = 2C_{mesh}\Delta x$. This meant that 95.45% ($d_i \leq 2\sigma$) of the Gaussian
 217 distribution was captured within the numerical simulation. It should be noted that σ is a tuning
 218 factor that should be adjusted to the particular circumstances under consideration.

219 The tangential F_t and normal F_n components of body forces acting on the fluid, which are in
 220 the opposite directions to the force acting on the blade, are given by

$$\begin{aligned}F_t &= F_L \sin \theta_{rel} - F_D \cos \theta_{rel}, \\ F_n &= F_L \cos \theta_{rel} + F_D \sin \theta_{rel}.\end{aligned}\quad (13)$$

221 Body force components acting on the fluid in x and y -axis directions are

$$\begin{aligned}F_x &= -F_t \sin \theta + F_n \cos \theta, \\ F_y &= F_t \cos \theta + F_n \sin \theta,\end{aligned}\quad (14)$$

222 where F_x is also the net thrust component of the fluid to the turbine. Note that $F_z = 0$, as three-
 223 dimensional flow effects on performance are neglected.

224 All the calculated force terms are then transformed into body force components, and passed
 225 back to OpenFOAM as momentum sources in the Navier-Stokes momentum equation for an
 226 incompressible Newtonian fluid given by:

$$\frac{D\vec{u}}{Dt} = -\frac{1}{\rho} \nabla p + \nu \nabla^2 \vec{u} + \frac{1}{\rho} \vec{F}, \quad (15)$$

227 in which \vec{u} is velocity field vector, ρ is fluid density, p is pressure, ν is the kinematic viscosity, t
 228 is time, and \vec{F} is the body force vector exerted on the fluid.

2.3. Power and Torque Calculation

The lift and drag force components acting on the blade exert an equal and opposite reaction on the flow [54]. This occurs at each point within the control volume V , which is a hollow cylinder of thickness 4σ with a radius equal to that of the rotor. This is used to calculate the instantaneous power output of the turbine at time t . L is blade length and dl is span-wise blade element dimension. The total torque acting on the fluid within the hollow cylindrical volume V is

$$\vec{\tau}_{fl} = \int^V \vec{r} \times \vec{F} dV. \quad (16)$$

The torque on the fluid acts in the opposite direction to the torque that turns the generator to create power τ_{pow} and the torque due to the moment of inertia of the blades τ_{bl} , such that $\tau_{fl} = -(\tau_{pow} + \tau_{bl})$. Here we have dropped the vector notation for torque, given that the torque vectors are all parallel to the z -axis. For a fixed-speed turbine,

$$\tau_{pow} = -\tau_{fl}. \quad (17)$$

Using the generator efficiency model from [56] to calculate power, we have

$$P_{real} = E_d E_g P_{ideal}, \quad (18)$$

where P_{real} is the actual power, E_d is the drive train efficiency, E_g is the generator and power conversion efficiency, and P_{ideal} is the instantaneous power output of the turbine.

2.4. Torque Control and Thrust

As with the original WATTES, the moment of inertia of the rotor must be defined with torque to accelerate the blades in WATTES-V. Here, it is assumed the majority of each blade's mass is at distance R , the rotor radius, from the centre of the rotor, and that each blade is identical to the other. The moment of inertia for a vertical-axis turbine can then be written as

$$I = N_{bl} m L R^2, \quad (19)$$

where N_{bl} is the number of blades, m is the mass per unit span, and L is the span length of each blade. We can then use I to define τ_{bl} , the torque that accelerates the blades. More details of this, and the time integration scheme used, can be found in [54].

The instantaneous thrust is calculated by integrating the x -direction body forces over the turbine control volume, that is

$$T = \int^V F_x dV. \quad (20)$$

3. Turbine Parameterization

Due to the lack of an experimental prototype, the present vertical-axis turbine model is validated against data from wind tunnel experiments involving a two-bladed H-type vertical-axis wind turbine (VAWT) that was equipped with sensors to measure thrust and side loading on the turbine [70]. The experimental data were collected at the Open Jet Facility at Delft University of Technology [70], which comprised a closed loop open jet air flow of 2.85 m \times 2.85 m outlet cross section. The wind tunnel test section was 13 m long. Table 1 lists the turbine model parameters, derived from [70].

The numerical model neglects the rotor shaft and support struts, and utilizes an unsteady Reynolds-averaged Navier-Stokes (URANS) formulation with k - ω shear stress transport (SST) turbulence closure scheme in OpenFOAM. The URANS approach is an attractive, computationally inexpensive prospect for far-wake simulation [55]. The k - ω SST turbulence model used is the original Menter model [71], which has been used successfully for many different types of flows. The SST (shear stress transport) turbulence model combines the k - ε model in the free shear flow, with the k - ω model in the near wall boundary regions. It is a robust two-equation eddy-viscosity turbulence model [71]. We would like further to develop our vertical-axis turbine model by adding solid support struts as a conventional turbine, which would enable our model to be used to represent

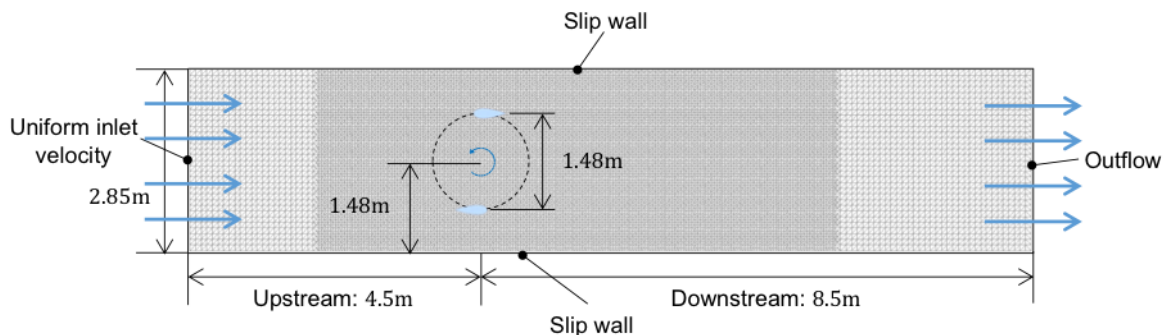
268 a wide range of vertical-axis turbines and turbine farms in the future. We thus chose to use a $k-\omega$
 269 SST model instead of a $k-\varepsilon$ model in this paper. Whilst there would be undoubted merit in exploring
 270 the effect of different turbulence models on the results, as undertaken by Barthelmie et al [72], this is
 271 beyond the scope of the present work, but is recommended for future study.

272 **Table 1.** VAT model parameters based on the experimental turbine configuration at Delft [70].

Property	Symbol	Value / Dimension
Number of blades	N_{bt}	2
Turbine diameter	D	1.48 m
Blade length	L	1.5 m
Aerofoil type	–	NACA 0021
Chord	c	0.075 m
Blade pitch	β_p	0°
Freestream flow speed	u_0	4.01 m/s
Fluid density	ρ	1.207 kg/m ³
Local Reynolds number	Re_c	19,838

273 The goal of the validation test is to check the ability of the newly developed numerical model
 274 WATTES-V to determine the thrust and side loading on the turbine for different values of azimuthal
 275 angle and tip speed ratio, with future applications to multi-bladed vertical-axis turbines in mind. This
 276 also enabled us to investigate the difference in behaviour between an idealised turbine with fixed tip-
 277 speed ratio and a more realistic turbine with torque control.

278 4. Results and Discussion



279 **Figure 3.** Computational mesh and boundary conditions, showing plan dimensions of the modelled
 280 domain.

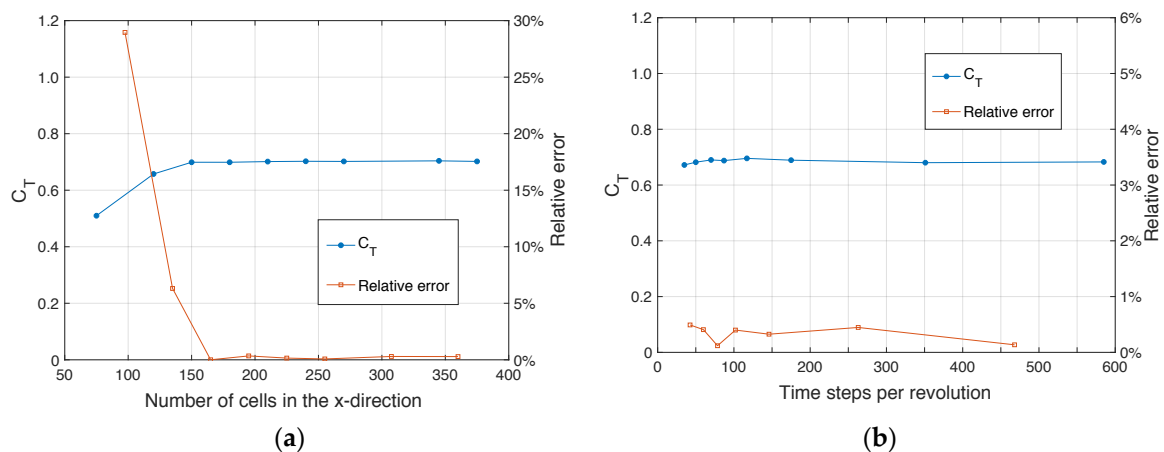
281 The three-dimensional (3D) computational domain is configured to be similar to the physical
 282 test-section containing the model-scale wind turbine [70]. The domain cross-sectional dimensions
 283 are 2.85 m \times 2.85 m, which match the outlet size of the flow contraction section located upstream of
 284 the open test section used in the experiments. However, given that the open test section allowed the
 285 flow to expand in the Open Jet Facility, it should be noted that the present computational domain
 286 (with straight side-walls not allowing the flow to expand) is likely to cause a blockage effect stronger
 287 than that in the experiments. The turbine is located 4.5 m downstream of the inlet, at mid elevation
 288 of the tunnel. Figure 3 shows a mesh slice in the x - y plane, generated using blockMesh and
 289 snappyHexMesh utilities in OpenFOAM. The mesh is refined by a factor of 2 using a hexahedral
 290 mesh in a rectangular region containing the turbine and near-wake field, following [73]. Here, mesh
 291 refinement is controlled by the number of cells in the (n_x, n_y, n_z) directions. Simulations were
 292 performed using the pimpleFoam solver, a merged PISO-SIMPLE algorithm. It should be noted that
 293 the azimuthal angle θ used in [70] starts from the y -axis, as indicated in the second figure in [70]. In

294 accordance with measurements from [70], the azimuth θ described in the following sections has
 295 been transformed to the experimental coordinate system.

296 Initial and boundary conditions are selected to be approximate those in the physical wind tunnel
 297 test section. The inflow velocity is fixed at 4.01 m/s inflow. Lateral, bottom, and top walls of the
 298 computational domain are represented numerically by slip-flow conditions. A zero pressure gradient
 299 is applied at the inlet, and a fixed pressure prescribed at the outlet with zero gradients for other flow
 300 variables. Inlet turbulence intensity is $\sim 10\%$, with turbulence kinetic energy k of $0.24 \text{ m}^2/\text{s}^2$ and
 301 specific dissipation rate ω of 1.78 s^{-1} . It should be noted that the computational time for a
 302 simulation of ten revolutions was about six core hours for a parallel computation using four
 303 computing cores.

304 4.1. Validation and Grid Sensitivity Studies

305 Sensitivity studies concerning spatial and temporal resolution will be discussed in this section.
 306 We first considered the convergence of turbine mean thrust coefficient for a tip-speed ratio of 3.3,
 307 shown in Figure 4. Mesh refinement is conducted by changing the number of cells in the x -direction
 308 with a fixed cell aspect ratio and mesh topology. The relative error [74] between the results from the
 309 two finest meshes is below 0.5% , indicating that mesh convergence had been achieved. The spatial
 310 mesh resolution is hitherto set to 150 cells in the stream-wise x -direction, with about 18 covering
 311 a single blade chord, (where the error between the finest mesh and the mesh employed is about 0.4%),
 312 giving a total number of 6.72×10^5 cells in the 3D simulation. Details of a mesh sensitivity study of
 313 the near-wake vorticity field are provided in the first part of Appendix B. Figure 4(b) displays time-
 314 step resolution test data, evaluated on the 3D grid with 150 cells in the x -direction. The relative
 315 error is below 0.5% , indicating low sensitivity to temporal resolution. In all these convergence tests,
 316 the Courant–Friedrichs–Lewy (CFL) number [75] is below 0.58. In this study, we employed $\Delta t =$
 317 0.03 s , corresponding to 120 time steps per revolution, giving a CFL number of 0.23. Simulations
 318 were carried out lasting at least 10 revolutions, with periodic convergence reached after 9
 319 revolutions when the difference in maximum turbine thrust between successive revolutions was
 320 0.06% .

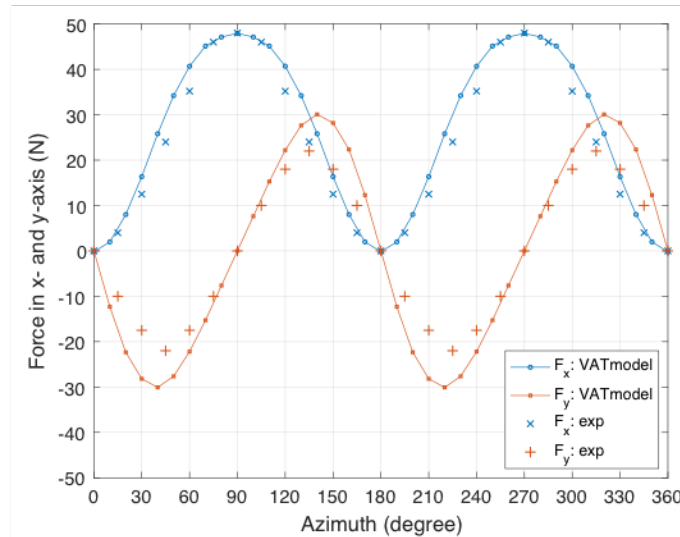


321 **Figure 4.** Resolution sensitivity of the VAT model: (a) Spatial resolution after 120 time steps per
 322 revolution; (b) Temporal resolution on a mesh with 150 cells in x -direction.

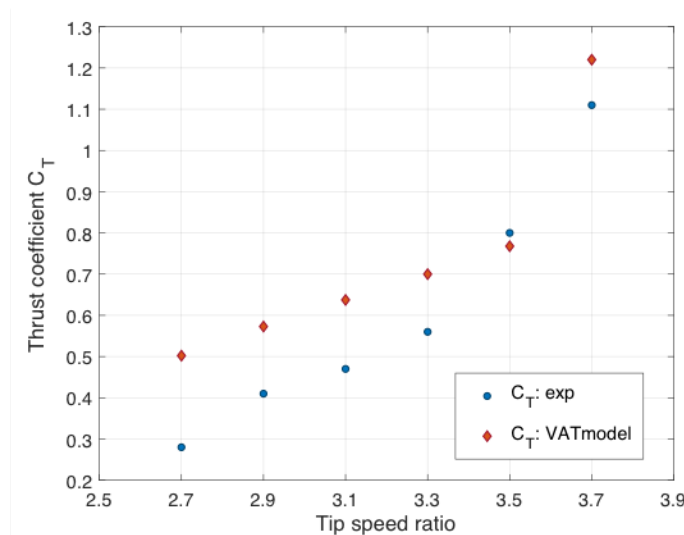
323 4.2. Two-Bladed H-Type Vertical-Axis Wind Turbine: Fixed Tip Speed Ratio

324 We now present results obtained for a two-bladed H-type vertical axis wind turbine where the
 325 tip speed ratio is set to a fixed value. Figure 5 compares the numerical predictions and measured
 326 thrust and lateral force components on the rotor for an incoming flow speed of 4.01 m/s, a fixed pitch
 327 angle of 0° , and a tip-speed ratio (TSR) of 3.7. The measurements were averaged over 22 turbine
 328 rotations. It can be seen that the numerical predictions and experimental measurements of the force

329 components in both x - and y - directions are similar in terms of amplitude and profile, with the
 330 maximum thrust loading experienced at the blade azimuth at 90° and 270° .

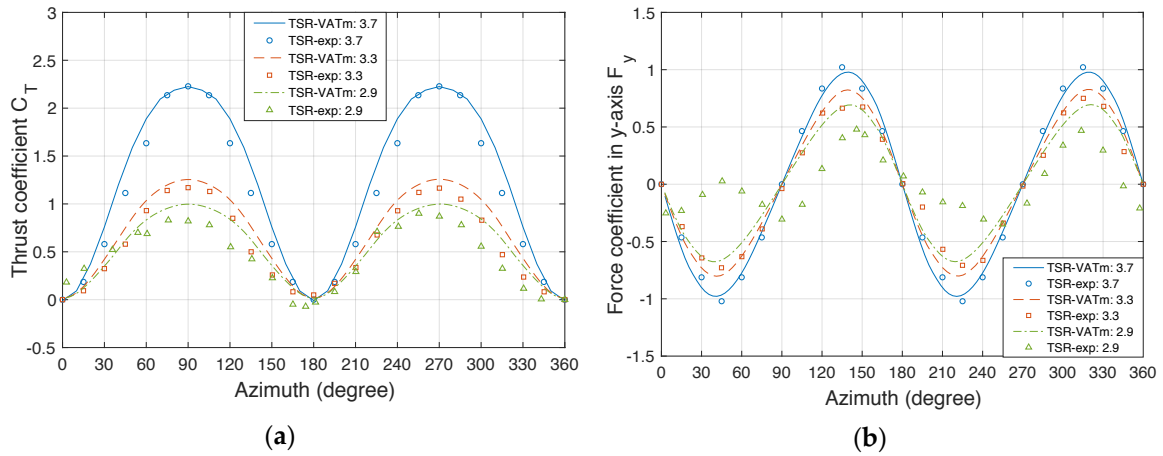


331 **Figure 5.** Comparison between predicted and measured [70] thrust and lateral forces on a wind
 332 turbine rotor of a two-bladed H-type vertical-axis wind turbine for an incoming flow speed of
 333 4.01 m/s, fixed pitch blade angle of 0° , and tip speed ratio of 3.7.



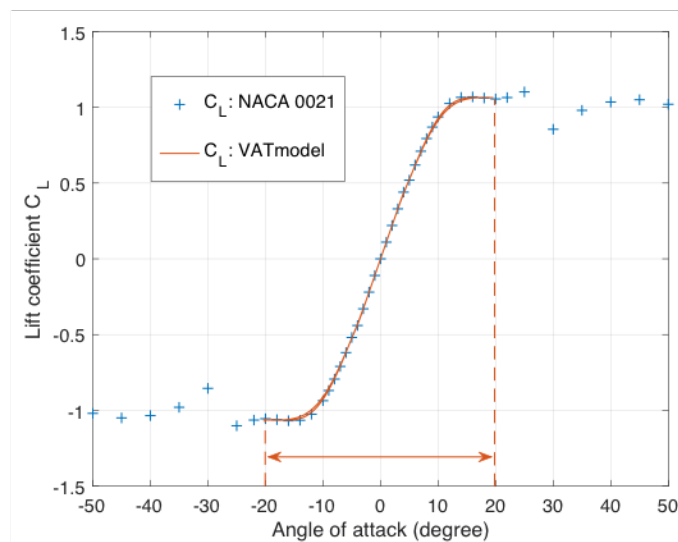
334 **Figure 6.** Comparison between predicted and measured [70] mean thrust coefficient C_T as a function
 335 of tip speed ratio in the range from 2.7 to 3.7, for a wind turbine rotor of a two-bladed H-type
 336 vertical-axis wind turbine with incoming flow speed of 4.01 m/s and fixed pitch blade angle of 0° .

337 We next study the effect of tip speed ratio on the mean thrust coefficient, carrying out numerical
 338 simulations that reproduce the experimental tip speed ratios of 2.7, 2.9, 3.1, 3.3, and 3.7. There is
 339 good overall agreement in the general trends of the model predictions and experimental data on the
 340 x -direction force coefficient as a function of TSR (Figure 6). The obvious overshoot is most likely
 341 caused by the blockage effect. The actual cross section of the experiments is supposed to be much
 342 wider than the outlet width of the open jet, where the blockage effect in the numerical simulations is
 343 stronger than in the experiments. A lack of information on the turbulence intensity of the wind tunnel
 344 experiments may also be a factor behind the discrepancy. Appendix B provides a more detailed
 345 discussion of the sensitivity of the model to inlet turbulence level and downstream domain length. It
 346 is found that the results are sensitive to inlet turbulence intensity, but not to a doubling of
 347 downstream domain length.



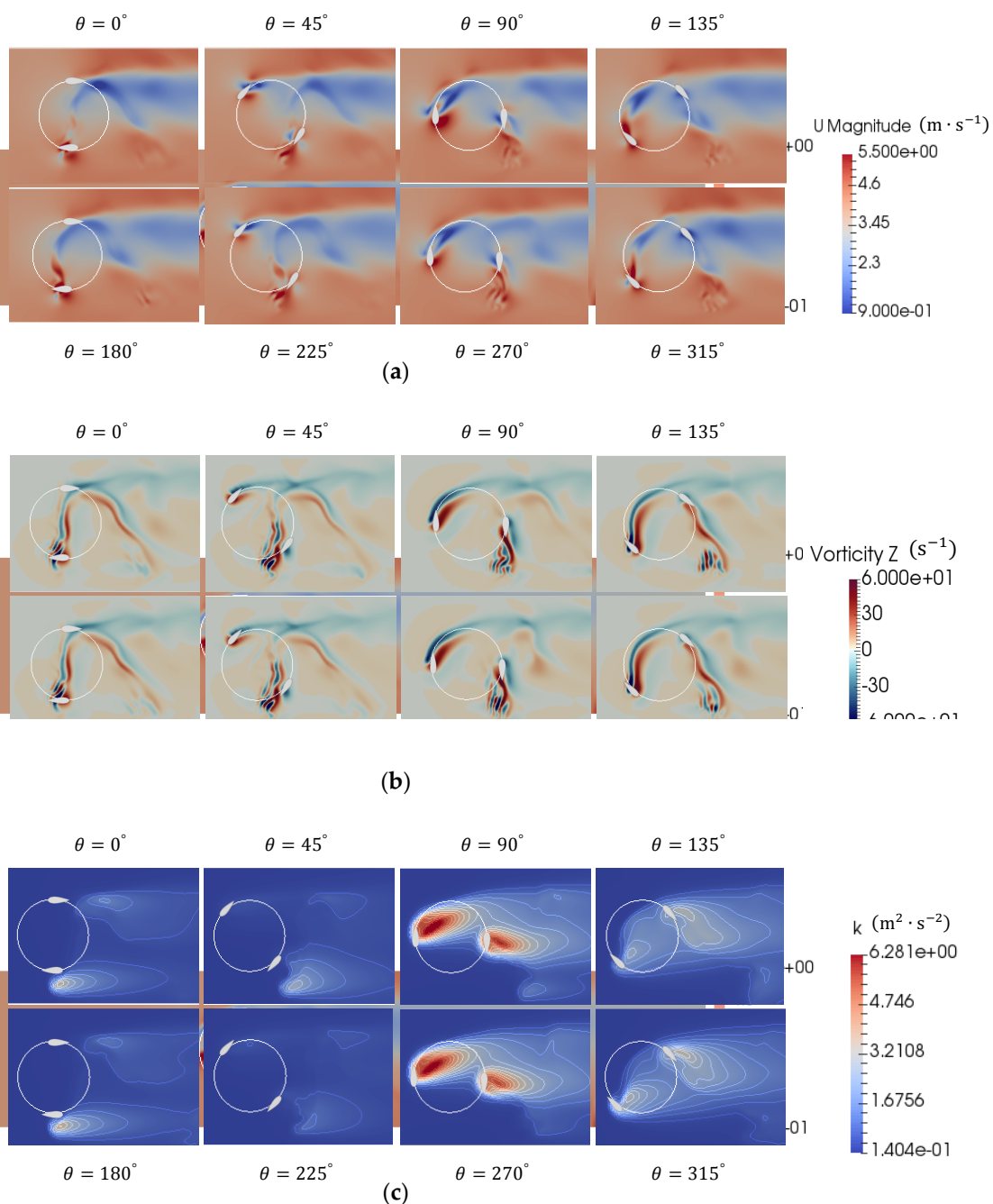
348 **Figure 7.** Comparison between predicted and measured [70] thrust and lateral force coefficients for
 349 different values of tip-speed ratio (TSR) (2.9, 3.3, and 3.7) as functions of azimuthal angle: (a) Thrust
 350 coefficient C_T ; and (b) Lateral force coefficient F_y .

351 Figure 7 depicts the variation in force coefficients in the x - and y - directions with azimuthal
 352 angle for three selected TSR values. Amplitudes of both the predicted and measured force coefficients
 353 increase progressively with TSR. This is because the blade velocity and hence the relative flow
 354 velocity experienced by the blades increase as TSR is raised; the increased velocities then augment
 355 the blade load. There appears to be satisfactory overall agreement between the numerical predictions
 356 and measurements of C_T and F_y for TSR values of 3.3 and 3.7. However, there are more noticeable
 357 discrepancies between the predicted and measured values of C_T and F_y for TSR 2.9; this is because
 358 the angle of attack exceeds the critical angle for parts of each rotation when TSR is 2.9, causing stall
 359 to occur.



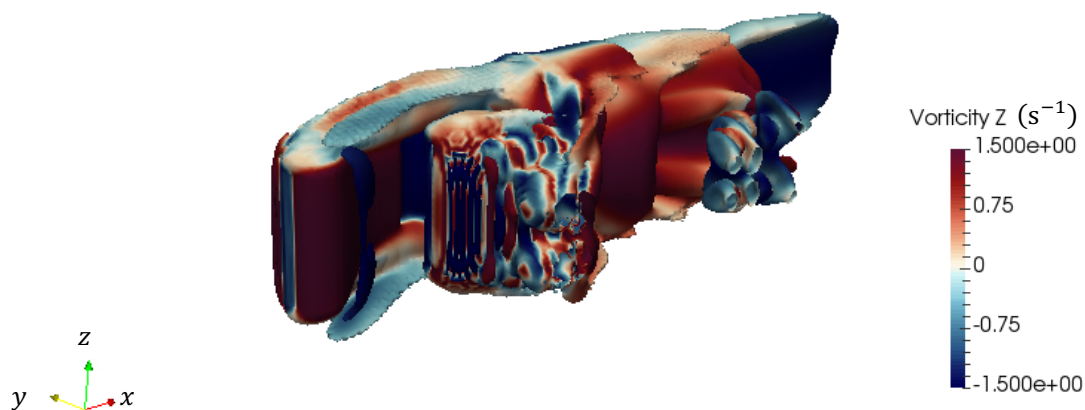
360 **Figure 8.** Lift coefficient as a function of local angle of attack at each grid point predicted by the VAT
 361 model for TSR = 2.9, compared with measurements for a static airfoil [76]; the red dashed lines show
 362 the range of local angle of attack.

363 Figure 8 illustrates the reduction in the lift coefficient that occurs at $TSR = 2.9$ as the critical angle
 364 of attack of the foil is exceeded at such a low value of TSR . It should be noted that data for cases where
 365 $TSR < 2.5$ were excluded from the experimental analysis because of this kind of poor aerodynamic
 366 performance [70]. The higher TSR values (i.e. > 2.9) considered in the validation case are sufficiently
 367 large to be outside the range in which dynamic stall is likely to occur, and the predicted and measured
 368 values of C_T and F_y almost match. However, as the local velocity of the blades increases, so does the
 369 local Reynolds number based upon chord length, Re_c , which in turn affects the dynamic performance
 370 of the airfoil. In future work, the dynamic stall problem could be solved for the modelled vertical-axis
 371 turbines by controlling the blade pitch to attain an even or higher pressure drop along the whole
 372 diameter of a rotor. As shown in Figure 8, the angle of attack on each blade does not exceed 20° at
 373 $TSR = 2.9$ (and higher), and so the dynamic stall problem is not encountered here.



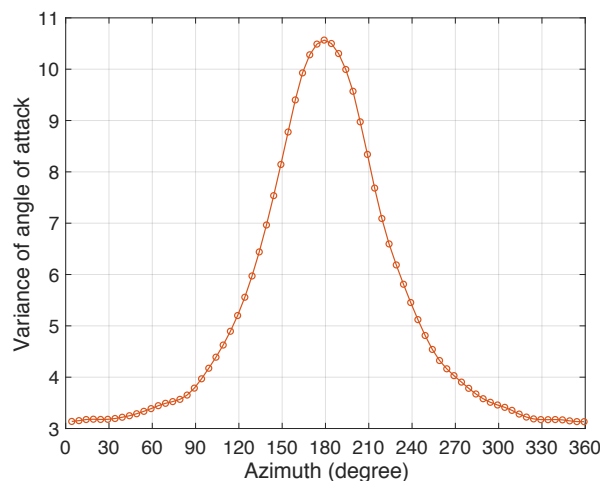
374 **Figure 9.** Flow patterns at eight different phases during a single revolution for $TSR = 3.7$: (a) Velocity
 375 magnitude (m/s); (b) z-component of vorticity (s^{-1}); and (c) Turbulence kinetic energy (m^2/s^2) in the
 376 central horizontal x - y plane.

377 Figure 9 shows plan views of the evolving velocity magnitude, vorticity z -component fields, and
 378 turbulence kinetic energy contours in the horizontal x - y plane at eight different phases during one
 379 revolution of the 2-bladed VAT operating at $TSR = 3.7$. The white blades are shown for interpretation
 380 only, and the k - ω SST model behaves like a k - ϵ model even near the blades (as in the free shear flow).
 381 θ is the azimuthal angle of the first blade measured from the experimental turbine in the anti-clockwise
 382 direction. The incoming flow passes through an annulus mapped out by the anti-clockwise rotating
 383 turbine, with vorticity generated on the surface of the blade and a turbulent wake developing
 384 downstream. The rotor interacts with its own wake, especially for azimuthal angles of 90° and 270° ,
 385 causing the thrust to increase. Vortex shedding starts to occur when the first rotor blade reaches an
 386 azimuthal position of about 180° . Vortices detach periodically from the turbine, and move to the
 387 downstream low-pressure wake field. This vortex shedding process drives oscillations in the local flow
 388 field affecting the forces on the rotor blades. The highest turbulence kinetic energy is observed at about
 389 90° or 270° of the azimuthal position.



390 **Figure 10.** Snapshot of vorticity iso-surfaces, coloured according to z -component.

391 Figure 10 illustrates an instantaneous three-dimensional vorticity field around the turbine. It can
 392 be seen that a smooth, quasi-two-dimensional shear layer, as a consequence of using URANS
 393 turbulence modelling, is created behind a blade moving towards the upstream direction. The blade
 394 then turns into the downstream direction and sheds large and more three-dimensional (spanwise-
 395 modulated) vortices. Strong tip vortices then interact with the shed vortices, and create a complex
 396 downstream wake field.



397 **Figure 11.** Variance of angle of attack as a function of azimuthal angle at $TSR = 3.7$.

398 Figure 11 shows the variance in angle of attack experienced by the two blades during a single
 399 revolution. This arises due to the blade shedding sheet vortices, which then break up into three-
 400 dimensional turbulence when the blade moves towards the downstream direction, giving greater

401 variation in the angle of attack across the blade. This highlights where the flow around the blades
 402 experiences strong variations, and this coincides with where vortex detachment occurs during each
 403 revolution.

404 The variance is calculated from:

$$\text{Var}(X) = E[X^2] - E[X]^2 = \sum_{i=1}^{N_{nd}} (p_i x_i^2) - \mu^2, \quad (21)$$

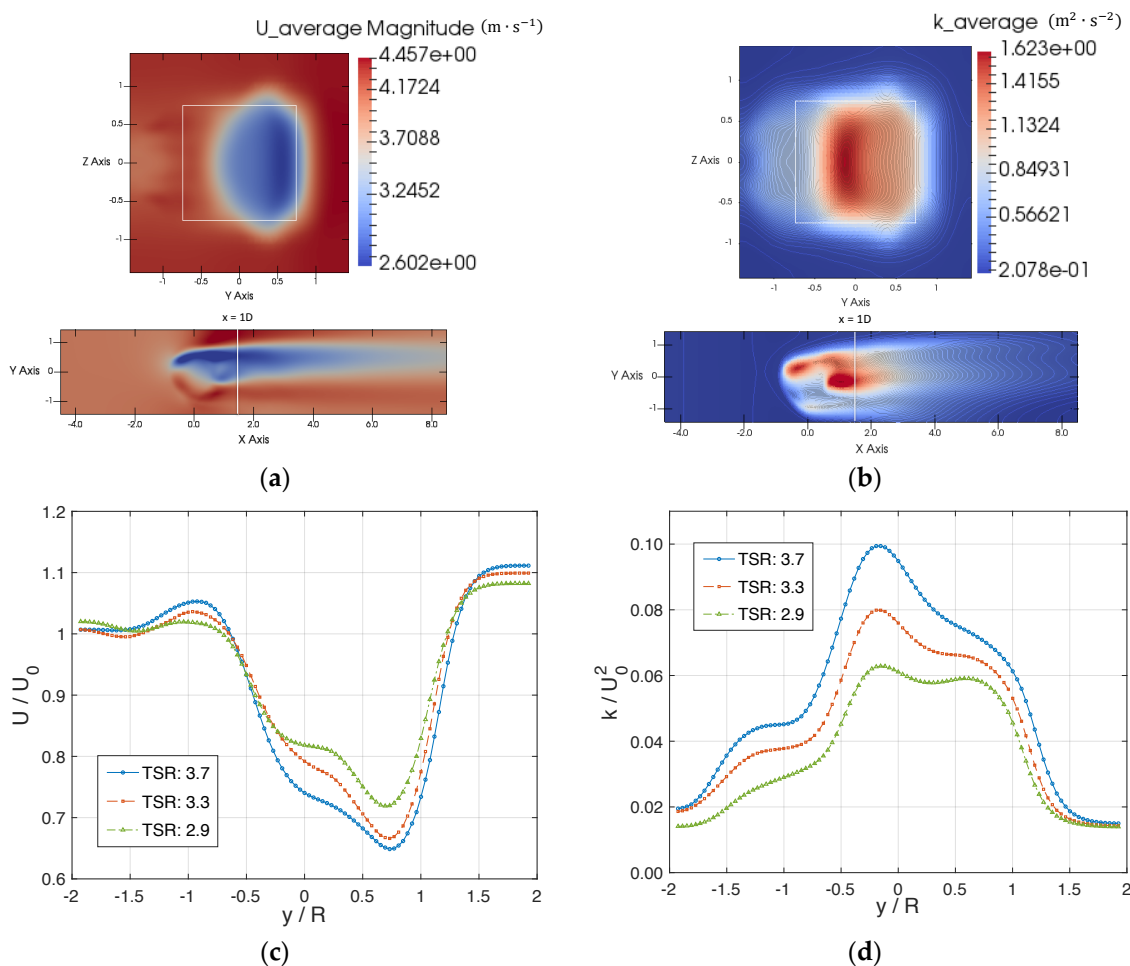
405 where X is a discrete random variable, E is an expectation operator, N_{nd} is the total number of nodes
 406 in the region of the blade, p_i is the probability mass function, α_i is the local angle of attack at point
 407 i , and $\mu = E[X]$ (or α) is the mean weighted value of angle of attack, given by

$$p_i x_i^2 = p_i \alpha^2 = \frac{\eta_i(d_i) \alpha_i^2}{\eta(d_i)} = \frac{\eta_i(d_i) \alpha_i^2}{\sum_{i=1}^{N_{nd}} \eta_i(d_i)}, \quad (22)$$

and

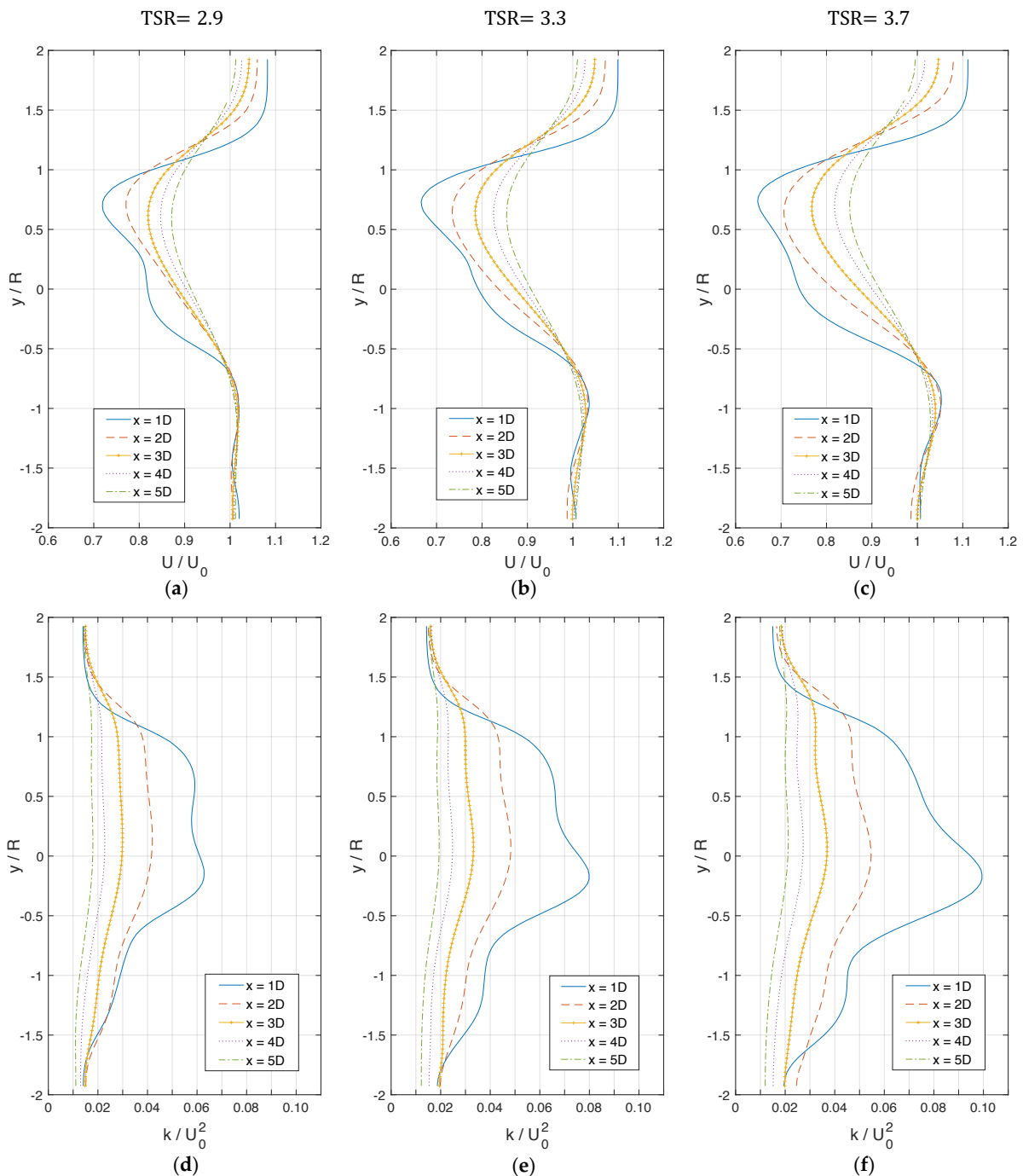
$$\mu = \frac{\sum_{i=1}^{N_{nd}} \eta_i(d_i) \alpha_i}{\eta(d_i)} = \frac{\sum_{i=1}^{N_{nd}} \eta_i(d_i) \alpha_i}{\sum_{i=1}^{N_{nd}} \eta_i(d_i)}. \quad (23)$$

408 A similar method was used in an earlier study [56]. The maximum variance occurs at the first
 409 rotor blade azimuth of 180° and the second blade azimuth of 0° or 360° (Figure 11). This three-
 410 dimensionality might be due to shear flow instability, which is similar to that observed for a 2D
 411 pitching airfoil when its angle of attack decreases. The variance profiles are asymmetric with
 412 azimuthal angle, with large changes occurring after vortex detachment.



413 **Figure 12.** Near wake flow at $x/D = 1$ and $z/H = 0$: (a) Slices through the mean velocity field in
 414 the y - z and x - y planes at $\text{TSR} = 3.7$; (b) Slices through the mean turbulence kinetic energy contours
 415 at $\text{TSR} = 3.7$; (c) Mean stream-wise velocity profiles for $\text{TSR} = 2.9, 3.3,$ and 3.7 ; and (d) Mean
 416 turbulence kinetic energy profiles for $\text{TSR} = 2.9, 3.3,$ and 3.7 .

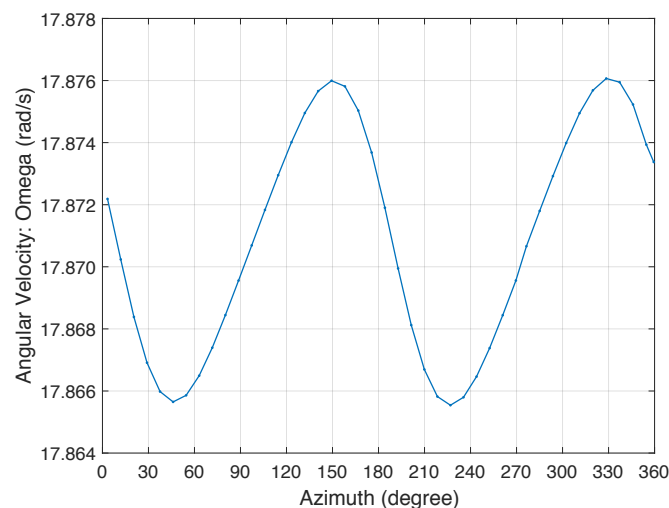
417 Figure 12 presents an overview of the downstream wake evolution behind the turbine with the
 418 distribution of the mean stream-wise velocity and the turbulence kinetic energy in the near-wake
 419 region at $x/D = 1$. The mean velocity field for $TSR = 3.7$, shown in Figure 12(a), is obviously
 420 asymmetric in the transverse (y) direction. The mean wake deficit in Figure 12(c) describes the
 421 characteristic of the mean velocity as it recovers rapidly on the coarse mesh [77–79] for the three
 422 selected tip speed ratios. Minimum values of mean velocities were found predominantly to occur at
 423 $y \sim 0.35D$. In the bypass flow at $y/R > 1.5$, the stream-wise velocity component reaches
 424 approximately $|U/U_0| = 1.1$, due to the blockage effect. Turbulence kinetic energy profiles in the
 425 vicinity of the rotor also exhibit clear asymmetry, with a peak at $y/R \sim -0.2$.



426 **Figure 13.** Horizontal profiles at mid-elevation of turbine $z/H = 0$: mean stream-wise velocity
 427 component (a) $TSR = 2.9$, (b) $TSR = 3.3$, (c) $TSR = 3.7$; and turbulence kinetic energy (d) $TSR = 2.9$,
 428 (e) $TSR = 3.3$, (f) $TSR = 3.7$.

429 Figure 13 shows the lateral profiles of stream-wise mean velocity (Figure 13(a)–(c)) and
 430 turbulence kinetic energy (Figure 13(d)–(f)) at $x = 1D - 5D$ downstream for TSR = 2.9, 3.3, and 3.7
 431 respectively. The near-wake region (roughly $x/D < 2$) is characterised by a low-momentum area
 432 isolated from the ambient flow in the presence of vortices, whereas the transition region (roughly
 433 $2 < x/D < 5$) is characterised by fast momentum recovery, high levels of turbulence, and expansion
 434 of the wake [80]. In Figure 13(a)–(c), the asymmetry of mean velocity profiles is more visible closer to
 435 the turbine centre in the near-wake region. In Figure 13(d)–(f), the mean turbulence kinetic energy
 436 profiles are W-shaped. The two peaks are in accordance with those of the mean velocity profiles;
 437 however, the maximum peak of the turbulence kinetic energy is located on the side with negative y ,
 438 not on the side with positive y where the largest velocity deficit is observed. This is presumably due
 439 to the (aforementioned) large vortices that shed when the blade motion is in the same direction as the
 440 flow velocity in this area. These vortices play a key role, and affect mixing between the ambient flow
 441 and the low-velocity wake flow. Comparing the shape of these wake deficits with results from other
 442 published models of vertical-axis turbines [30,80], it can be stated that these characteristics of the
 443 mean velocity and turbulence kinetic energy profiles agree qualitatively with these previous studies
 444 of vertical-axis turbine wakes. For example, the shape of the mean stream-wise velocity profile of the
 445 present model corresponds well with those of experimental profiles presented in Figure 9 (left) in [30]
 446 and Fig. 5. (a) in [80], where the lowest values of U/U_0 are both located close to $y = 0.35D$. The shape
 447 of the turbulence kinetic energy profile exhibits good agreement with the experimental profile in
 448 Figure 9 (right) in [30], especially for areas in the vicinity of both peaks, and is in even better
 449 accordance than the University of New Hampshire reference vertical-axis turbine (UNH-RVAT)
 450 model used in [30]. For the Edinburgh turbine (see Figure 1), the bending stresses at both ends are
 451 decreased by a factor of nearly four, with the red rings suppressing tip-vortex losses caused by the
 452 adjacent foils at different angles. Although the rings experience drag, the spoked wheel could well
 453 be a more efficient load-bearing structure than a tower, which experiences vortex shedding in
 454 addition to drag [65].

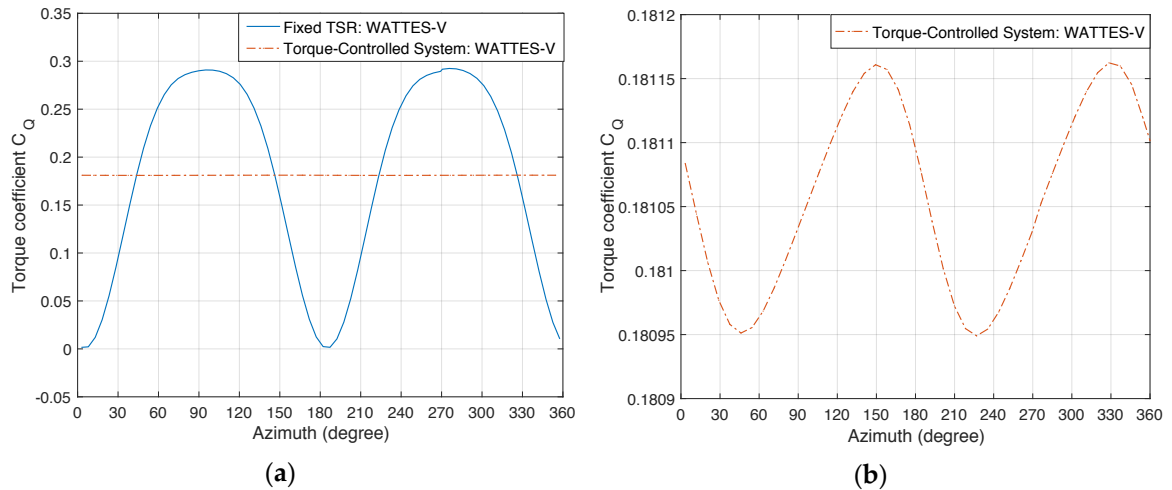
455 4.3. Two-Bladed H-Type Vertical-Axis Wind Turbine: Torque-Controlled Tip Speed Ratio



456 **Figure 14.** Variation of angular velocity ω as a function of azimuthal angle in the torque-controlled
 457 system at TSR = 3.3.

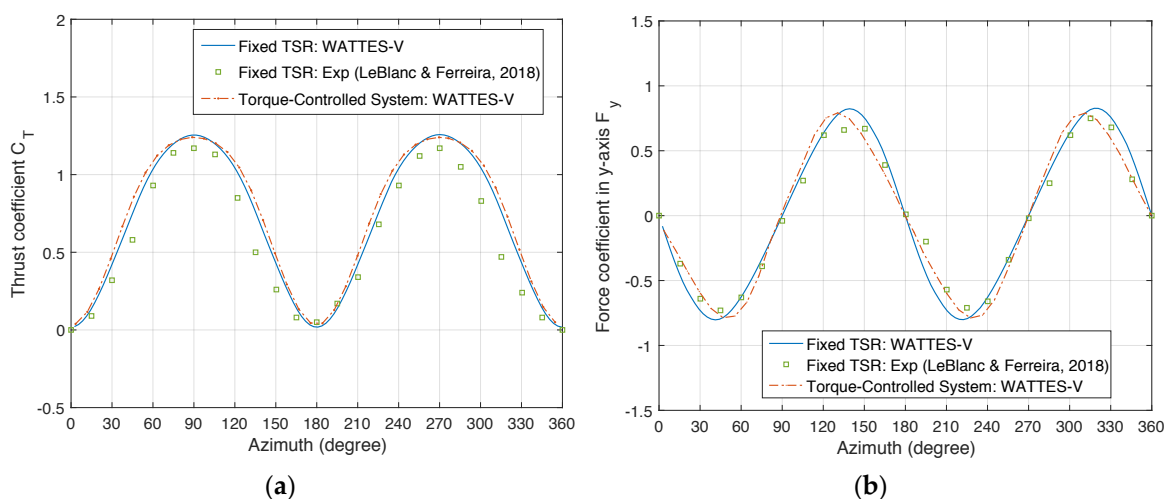
458 We now present results obtained for a two-bladed H-type vertical axis wind turbine where the
 459 rotational speed of the blades is controlled by the torque. Figure 14 shows the limit cycle variation of
 460 the turbine angular velocity against azimuthal angle of the first blade, where the rotor is dynamically
 461 driven by the incoming wind flow. The predicted mean angular velocity ω in the torque-controlled
 462 model is 17.87 rad/s . This value is slightly smaller than that of the initial angular velocity (of
 463 17.88 rad/s , calculated from $\omega_{ini} = \frac{\text{TSR} \cdot u_0}{R}$) used to set the rotor in motion. In general, the turbine

464 settles down until the energy losses due to drag and the generator are balanced by the energy
 465 extracted from the fluid through lift.



466 **Figure 15.** Variation of torque coefficient C_Q as a function of azimuthal angle at TSR = 3.3: (a)
 467 Comparison between results from the model with fixed TSR and its torque-controlled counterpart; (b)
 468 Enlarged zone of C_Q variation in the torque-controlled model.

469 The torque coefficient C_Q is calculated by using the dynamic generator torque data as $C_Q =$
 470 $\frac{\tau_{pow}}{\frac{1}{2} \rho u_0^2 (D L) R}$. Figure 15 shows a comparison of the torque coefficient results obtained for the fixed tip-
 471 speed ratio and torque-controlled cases. As shown in Figure 15(a), the predicted C_Q for the model
 472 with fixed tip-speed ratio keeps changing through one rotor-revolution, whereas the C_Q for the
 473 torque-controlled model remains almost constant with azimuthal angle. Figure 15(b) presents an
 474 enlarged graph of C_Q variation for the torque-controlled case, where C_Q experiences less than 0.1%
 475 change with azimuthal angle. This can be explained by the high mass density of the blades, whose
 476 angular momentum becomes a source of torque for the generator when fluid torque drops. This
 477 behaviour is not present in the fixed tip-speed model, as the torque accelerating the blades is by
 478 necessity always zero.



479 **Figure 16.** Comparison between predicted (including the model with fixed TSR and the torque-
 480 controlled model) and measured [70] thrust and lateral force coefficients for TSR= 3.3 as functions of
 481 azimuthal angle: (a) thrust coefficient C_T ; and (b) lateral force coefficient F_y .

482 Figure 16 displays the thrust and lateral force coefficients as functions of the azimuthal angle
 483 obtained from the fixed tip-speed ratio model, the measured data [70], and the torque-controlled

484 model (where the thrust derives purely from the aerodynamic flow driving the turbine). Satisfactory
485 overall agreement can be seen between the numerical predictions and measurements of C_T and F_y
486 for TSR values of 3.3, as shown in Figure 16(a)(b). However, there are still some noticeable
487 discrepancies evident between the torque-controlled model predictions, the fixed tip-speed ratio
488 model predictions, and the experimental measurements, especially regarding F_y in Figure 16(b).

489 5. Conclusions

490 This paper has presented a newly developed, efficient, parallelised, numerical model that
491 simulates turbulent flow through vertical-axis turbines with a torque-controlled system, as well as
492 with a fixed tip-speed ratio system. This computationally efficient numerical model WATTES-V of a
493 single cross-flow turbine was developed within the OpenFOAM CFD framework. The model is based
494 on actuator line theory, and combines classical blade element theory, an unsteady Reynolds-averaged
495 Navier–Stokes flow model, and a $k-\omega$ SST turbulence model.

496 This numerical model with fixed tip-speed ratio was validated against experimental data
497 acquired from an H-type 2-bladed vertical-axis wind turbine [70]. The model gives numerical
498 predictions in satisfactory overall agreement with experimental data on thrust and lateral loading. It
499 is planned that the present cross-flow turbine model will be employed in future research on wakes
500 behind close-packed contra-rotating vertical-axis tidal turbines [12]; hence, the support struts and
501 tower shaft for a normal H-type vertical-axis turbine have not been considered herein. The present
502 results show that vortex shedding occurs at the azimuthal position of the first rotor blade, at about
503 180° . Vortices detach periodically from the turbine, and the resulting interactions create a complex
504 downstream wake. The angle of attack for each blade did not exceed 20° in the present study, and
505 so dynamic stall could be ignored. However, for future studies based on the present numerical model,
506 either a dynamic stall model could be added as a correction, or a pitch-controlled system could be
507 used to limit the angle of attack to an optimum value.

508 The wake field predicted by the present vertical-axis turbine model with fixed tip-speed ratio
509 may be divided into two distinct regions. The near-wake region features a low-momentum zone
510 where vortices shed from the turbine have a significant influence on the low-velocity region. The
511 wake deficit in the transitional-wake region exhibits momentum recovery due to entrainment of
512 ambient flow into the wake, and generates asymmetric velocity profiles about the wake centreline.
513 Analysis of wake turbulence behind a single vertical-axis turbine could facilitate better
514 understanding of key flow features that contribute to wake recovery behind an array of close-packed
515 contra-rotating vertical-axis turbines in future work. The sensitivity study on the turbulence
516 parameters of the inlet flow and the downstream domain length (discussed in the Appendix B)
517 should be useful for future experimental tests and numerical validations.

518 Dynamic predictions made by the present numerical model with torque-controlled tip-speed
519 ratio are in satisfactory overall agreement with corresponding results from the fixed tip-speed ratio
520 model and experimental data [70] on thrust and lateral loading. In the former case, the rotor is
521 demonstrably driven by the blade-generated lift, which is counteracted by the torque that accelerates
522 the blades and turns the generator. The present model should be useful in the future by enabling
523 predictions of the dynamic response of practical vertical-axis turbines to unsteady flow.

524 **Author Contributions:** Funding acquisition, V.V; Investigation, R.Z; Methodology, R.Z and A.C.W.C;
525 Supervision, A.C.W.C, A.G.L.B, T.N and V.V; Writing—original draft, R.Z; Writing—review & editing, A.C.W.C,
526 A.G.L.B and T.N.

527 **Funding:** This research was funded by Flowturb project.

528 **Acknowledgments:** The first-named author is supported by funding awarded by the China Scholarship Council
529 and the University of Edinburgh. The authors thank Prof. Stephen Salter for insightful suggestions that have
530 informed the present research. The work was partly funded by the UK Engineering and Physical Sciences
531 through the FloWTurb project (EP/N021487/1).

532 **Conflicts of Interest:** The authors declare no conflict of interest.

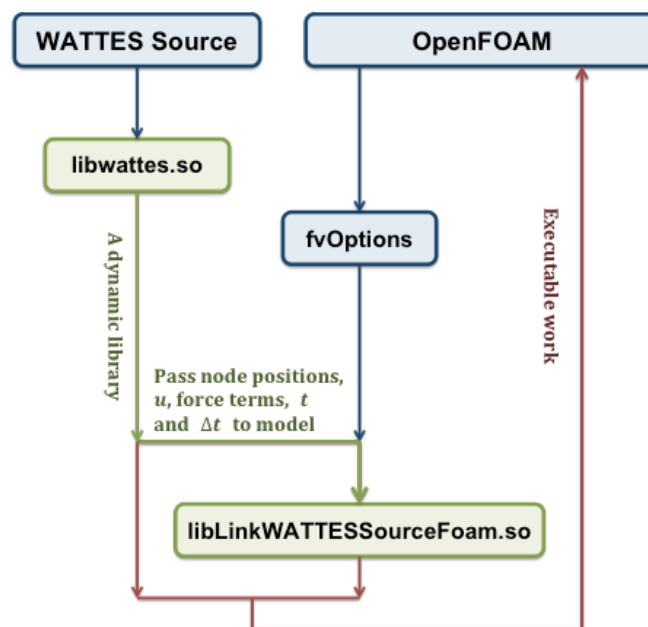
533 Nomenclature

Variable	Description
c	Blade chord (m)
C_L, C_D	Lift and drag coefficients
d_i	Smallest distance between a given point and the i^{th} actuator line (m)
\vec{e}_L, \vec{e}_D	Unit vectors in lift and drag directions
E_d, E_g	Drive train efficiency, conversion efficiency
f_L, f_{L_i}	Lift component per unit span on the i^{th} blade (N/m)
f_D, f_{D_i}	Drag component per unit span on the i^{th} blade (N/m)
F_L, F_D	Turbine lift and drag forces per unit span (N/m)
F_t, F_n	Tangential and normal forces per unit span (N/m)
F_x, F_y	Body forces per unit span in x - and y -axis directions (N/m)
I	Moment of inertia ($\text{kg} \cdot \text{m}^2$)
L	Blade length (m)
m	Blade mass per unit span (kg/m)
N_{bl}	Number of blades
P_{real}, P_{ideal}	Actual power, instantaneous power (W)
r	Radial distance from the rotor centre (m)
Re	Reynolds number
T	Thrust (N)
u	Local inflow velocity (m/s)
u_0	Freestream velocity (m/s)
u_{bl}	Blade velocity (m/s)
u_{rel}	Flow relative velocity (m/s)
u_{az}	Azimuthal component of the fluid velocity (m/s)
u, v, w	Three components of local velocity (m/s)
(x, y, z)	Coordinates in the original reference frame (m)
(x', y', z')	Coordinates in the blade reference frame (m)
α	Angle of attack (rad)
β	Corrected pitch (rad)
β_p	Blade pitch (rad)
β_t	Local blade twist angle (rad)
η_i	Gaussian regularization
θ	Azimuthal angle (rad)
θ_{rel}	Relative angle (rad)
ρ	Fluid density (kg/m^3)
σ	Width of the Gaussian kernel
$\tau_{fl}, \tau_{pow}, \tau_{bl}$	Fluid torque, generator torque, blade torque ($\text{N} \cdot \text{m}$)
ω_{bl}	Blade angular velocity (rad/s)
$\dot{\omega}$	Blade angular acceleration (rad/s ²)

534 Appendix A

535 Model Architecture

536 The Wind and Tidal Turbine Embedded Simulator (WATTES) [56,54] code is an open library
 537 source code written in Fortran 95, which employs both the dynamic torque-controlled actuator disc
 538 and the actuator line methods with active-pitch correction to simulate the behaviour of multiple wind
 539 and tidal horizontal-axis turbines, together with a simplified generator model. Compared with other
 540 momentum codes, WATTES predicts the dynamic response of the device to the flow, with lift and
 541 drag force components balanced by inertial effects and the resistive torque induced by the generator.
 542 Force components are incorporated within the incompressible Navier-Stokes momentum equations
 543 as body force components [54]. For computational efficiency, WATTES exploits parallel
 544 programming based on multiple instructions multiple data (MIMD) [52] through the Message
 545 Passing Interface protocol (MPI). The solution is computed on a number of processors that function
 546 asynchronously and independently. The original WATTES model simulated flows using Fluidity,
 547 which is an open-source hr-adaptive multiphase computational fluid dynamics (CFD) solver based
 548 on an unstructured finite element method and offers anisotropic mesh refinement, developed mainly
 549 by researchers at Imperial College London [81]. The original WATTES source code was used to
 550 represent horizontal-axis turbines within the OpenFOAM [65] CFD framework, and formed the basis
 551 of the modified numerical model WATTES-V used herein to simulate flow past a vertical-axis turbine.
 552 OpenFOAM is freely available open-source CFD software based on the finite volume method on
 553 general unstructured polyhedral meshes, and is written in C++. In order to benefit from the
 554 advantages provided by the original WATTES source code, proper coupling of WATTES and
 555 OpenFOAM was a necessary prerequisite before the further development of WATTES-V model
 556 described in the present study.



557 **Figure A1.** Flow chart of coupled OpenFOAM-WATTES program.

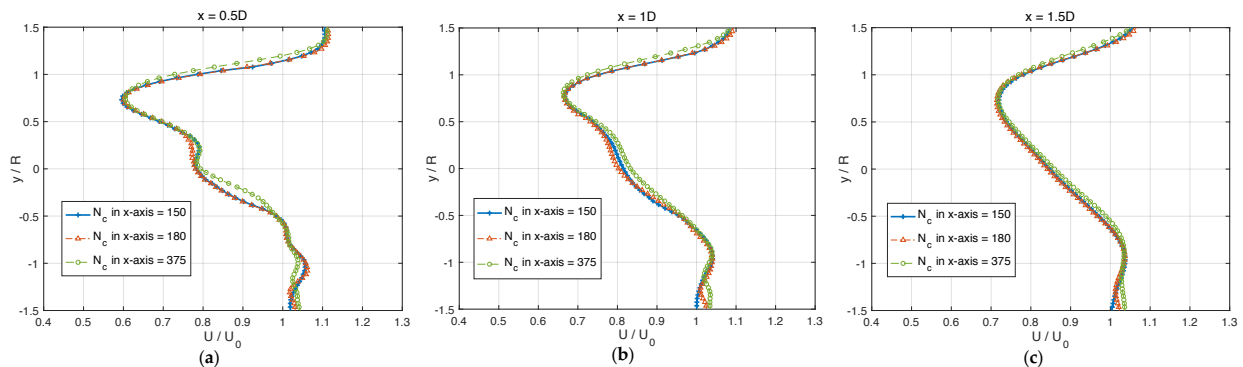
558 The flow chart in Figure A1 summarises the coupled OpenFOAM-WATTES procedure. The
 559 main structure of OpenFOAM comprises four main directories: core OpenFOAM libraries (named
 560 src), solvers and utilities (applications), test cases that demonstrate a wide-range of OpenFOAM
 561 functionality (tutorials), and documentation (named doc). OpenFOAM is a collection of
 562 approximately 250 applications built upon a collection of over 100 software libraries (modules). Each
 563 application performs a specific task within a CFD workflow. Case setup is described by steering a
 564 collection of files in a tutorial directory, providing details of the mesh, physical models, solver, post-
 565 processing controls, etc. To couple the WATTES model with OpenFOAM, an interface program
 566 linking WATTES model was written in the src directory via a dynamic library with wrapper functions.
 567 The velocity field and momentum sources of the WATTES model were mapped to correspond

568 correctly with those in OpenFOAM. A new fvOptions framework is introduced for run-time
 569 selectable physics by representing the force components from the WATTES model as momentum
 570 sources in the governing equations in OpenFOAM.

571 Appendix B

572 This Appendix presents results from tests which examine the influence of mesh convergence on
 573 the vorticity field in the near wake, the choice of inlet turbulence parameter, and the length of the
 574 downstream domain dimension.

575 Effect of Mesh Convergence on Near-Wake Vorticity Field



576 **Figure B1.** Horizontal profiles computed on three meshes of normalised mean stream-wise velocity
 577 component at turbine mid-height where $z/H = 0$ at (a) $x = 0.5D$, (b) $x = 1D$, and (c) $x = 1.5D$.

578 Figure B1 presents horizontal profiles of turbine mean streamwise velocity at a tip-speed ratio
 579 of 3.3 in the near-wake region computed on coarse, medium, and fine meshes (with $N_x = 150$, $N_x =$
 580 180 , and $N_x = 375$ cells respectively in the x -direction). The figure illustrates model sensitivity to
 581 spatial resolution. Satisfactory agreement is generally achieved between the profiles obtained on the
 582 different meshes, although some slight discrepancies are evident, the relative two-norm errors [56]
 583 are 2.80%, 2.44%, 1.94% respectively, which are all under 3% and are within acceptable margins.
 584 We find that a spatial grid resolution of 150 cells in the x -direction, giving a total number of
 585 6.72×10^5 cells in a 3D simulation, is sufficient to achieve mesh convergence.

586 Sensitivity Analysis concerning Inlet Turbulence Parameters

587 Turbulence intensity (TI) is defined as the ratio of the root-mean-square of flow velocity
 588 fluctuations $u' \equiv \sqrt{\frac{1}{3}(u_x'^2 + u_y'^2 + u_z'^2)}$ to the mean flow speed $U \equiv \sqrt{U_x^2 + U_y^2 + U_z^2}$ [48], and is
 589 expressed:

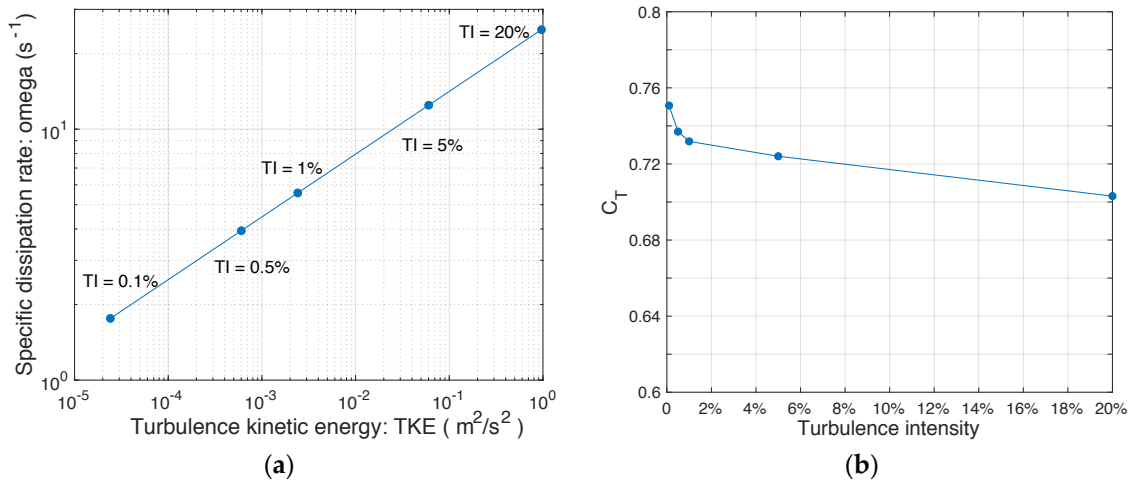
$$\text{TI} \equiv \frac{u'}{U} = \sqrt{\frac{2}{3} \cdot \frac{k}{U^2}} \quad (\text{B1})$$

590 where k is turbulence kinetic energy (TKE). A value for TKE at the inlet is thus calculated from
 591 Equation (B1) for a given TI [82]. The specific dissipation rate ω used in the k - ω SST turbulence
 592 model in OpenFOAM is calculated using the following formula [83]:

$$\omega = \frac{k^{0.5}}{C_\mu l'} \quad (\text{B2})$$

593 where C_μ is a turbulence model constant equal to 0.09, and l' is the turbulence length scale.

594 Sensitivity of the results to the inlet turbulence parameters is examined by setting different inlet
 595 values of k and ω calculated from Equations (B1) and (B2) for a range of turbulence intensity values
 596 from 0.1% to 20%, with TSR = 3.3. The results are shown in Figure B2.

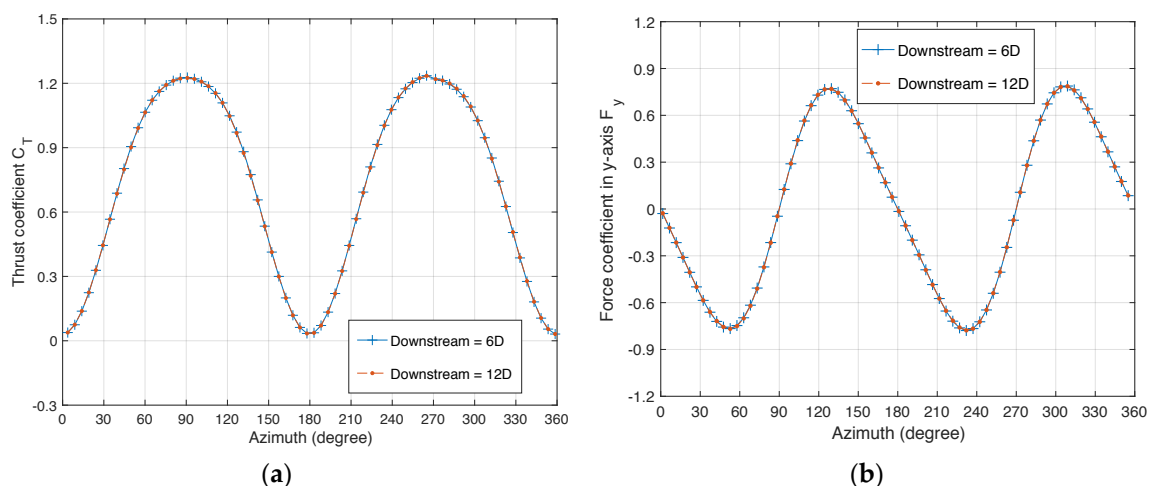


597 **Figure B2.** Inlet turbulence conditions and their effects on the vertical-axis turbine model for TI =
 598 0.1%, 0.5%, 1%, 5%, and 20%: (a) specific dissipation rate (ω) versus turbulence kinetic energy
 599 (TKE or k), and (b) thrust coefficient versus TI.

600 Figure B2 displays the variation of specific dissipation rate with turbulence kinetic energy, and
 601 the thrust coefficient with turbulence intensity for the vertical-axis turbine model. It can be seen that
 602 the mean thrust coefficient tends to decrease as TI increases. In particular, as TI varies from 0.1% to
 603 20%, the thrust coefficient decreases by 6.34%. This indicates that the choice of level of turbulence
 604 intensity at the inlet can have a substantial effect on the thrust value of a vertical-axis turbine.
 605 However, the change of thrust coefficient is only about 1.72% for a more realistic range of TI between
 606 1% and 10%.

607 Sensitivity Analysis concerning Downstream Domain Size

608 To investigate the impact of the limited downstream domain size on the results, we doubled the
 609 stream-wise length of the downstream domain, for a case of fixed TSR = 3.3, and compared the thrust
 610 and lateral force coefficients obtained using the two domains.



611 **Figure B3.** Comparison of predicted force coefficients obtained on meshes of downstream length 6D
 612 and 12D, for TSR = 3.3 as functions of azimuthal angle: (a) thrust coefficient C_T ; and (b) lateral force
 613 coefficient F_y .

614 Figure B3 shows that very satisfactory agreement is obtained for the values of C_T and F_y on the
 615 two domains, for a fixed TSR = 3.3; relative errors between the coefficients obtained using the
 616 different domains lie below 0.057%. This confirms that the downstream length utilized in the main
 617 paper is adequate.

618 **References**

- 619 1. IEA. *Energy and Climate Change*; World Energy Outlook Special Report; Paris, France, IEA: 2015; Volume
620 479, pp. 1–200.
- 621 2. EIA. *International Energy Outlook 2017*; U.S. Energy Information Administration, Office of Energy Analysis,
622 US Department of Energy: Washington, DC, USA, 2017; p. 20585.
- 623 3. Borthwick, A.G.L. Marine Renewable Energy Seascape. *Engineering* **2016**, *2*, 69–78.
- 624 4. International Energy Agency. *Solutions for the 21st Century*; International Energy Agency, Paris, France,
625 2002.
- 626 5. Wong, K.H.; Chong, W.T.; Sukiman, N.L.; Poh, S.C.; Shiah, Y.-C.; Wang, C.-T. Performance enhancements
627 on vertical axis wind turbines using flow augmentation systems: A review. *Renew. Sustain. Rev.* **2017**, *73*,
628 904–921.
- 629 6. Salter, S.H. Are nearly all tidal stream turbine designs wrong? In Proceedings of the 4th International
630 Conference on Ocean Energy, Dublin, Ireland, 17–19 October 2012.
- 631 7. Sutherland, H.J.; Berg, D.E.; Ashwill, T.D. *A Retrospective of VAWT Technology*; Technical report, Sandia
632 Report, SAND2012-0304; Sandia National Laboratories: Albuquerque, NM, USA, 2012.
- 633 8. Strom, B.; Johnson, N.; Polagye, B. Impact of blade mounting structures on cross-flow turbine performance.
634 *J. Renew. Sustain. Energy* **2018**, *10*, 034504.
- 635 9. Sahim, K.; Santoso, D.; Puspitasari, D. Investigations on the effect of radius rotor in combined Darrieus-
636 Savonius wind turbine. *Int. J. Rotating Mach.* **2018**, *2018*, 3568542.
- 637 10. Subramanian, A.; Yogesh, S.A.; Sivanandan, H.; Giri, A.; Vasudevan, M.; Mugundhan, V.; Velamati, R.K.
638 Effect of airfoil and solidity on performance of small scale vertical axis wind turbine using three
639 dimensional CFD model. *Energy* **2017**, *133*, 179–190.
- 640 11. Dyachuk, E. Aerodynamics of Vertical-Axis Wind Turbines-Development of Simulation Tools and
641 Experiments. Ph.D. Thesis, Uppsala University, Uppsala, Sweden, 2015.
- 642 12. Salter, S.H.; Taylor, J.R.M. Vertical-axis tidal-current generators and the Pentland Firth. *IMEchE J. Power*
643 *Energy* **2006**, *221*, 181–199.
- 644 13. Suffera, K.H.; Usubamatov, R.; Quadirc, G.A.; Ismail, K. Modeling and numerical simulation of a vertical
645 axis wind turbine having cavity vanes. In Proceedings of the 5th International Conference on Intelligent
646 Systems, Modelling and Simulation, IEEE, Langkawi, Malaysia, 27–29 January 2014.
- 647 14. Dillmann, A.; Heller, G.; Klaas, M.; Kreplin, H.P.; Nitsche, W.; Schröder, W. *New Results in Numerical and*
648 *Experimental Fluid Mechanics VII*; Contributions to the 16th STAB/DGLR Symposium Aachen, Germany
649 2008.
- 650 15. Hameed, M.S.; Shahid, F. Evaluation of aerodynamic forces over a vertical axis wind turbine blade through
651 CFD analysis. *J. Appl. Mech. Eng.* **2012**. doi:10.4172/2168-9873.1000116.
- 652 16. Almohammadi, K.M.; Ingham, D.B.; Ma, L.; Pourkashanian, M. CFD sensitivity analysis of a straight-blade
653 vertical axis wind turbine. *Wind Eng.* **2012**, *36*, 5, 571–588.
- 654 17. Ghatage, S.V.; Joshi, J.B. Optimisation of vertical axis wind turbine: CFD simulations and experimental
655 measurements. *Can. J. Chem. Eng.* **2012**, *90*, 1186–1201.
- 656 18. Zhang, L.X.; Liang, Y.B.; Liu, X.H.; Jiao, Q.F.; Guo, J. Aerodynamic performance prediction of straight-
657 bladed vertical axis wind turbine based on CFD. *Adv. Mech. Eng.* **2013**, *5*, 905379.
- 658 19. Muneer, A.; Khan, M.B.; Sarwar, U.B.; Khan, Z.A.; Badar, M.S. CFD analysis of a Savonius Vertical axis
659 wind turbine. In Proceedings of the 2015 Power Generation Systems and Renewable Energy Technologies,
660 Islamabad, Pakistan, 10–11 June 2015.
- 661 20. Asim, T.; Mishra, R.; Kaystha, S.; Aboufares, G. Performance comparison of a vertical axis wind turbine
662 using commercial and open source computational fluid dynamics based codes. In Proceedings of the
663 International Conference on Jets, Wakes and Separated Flows, Stockholm, Sweden, 16–18 June 2015.
- 664 21. Alaimo, A.; Esposito, A.; Messineo, A.; Orlando, C.; Tumino, D. 3D CFD Analysis of a Vertical Axis Wind
665 Turbine. *Energies* **2015**, *8*, 3013–3033.
- 666 22. Bai, C.J.; Lin, Y.Y.; Lin, S.Y.; Wang, W.C. Computational fluid dynamics analysis of the vertical axis wind
667 turbine blade with tubercle leading edge. *J. Renew. Sustain. Energy* **2015**, *7*, 033124.
- 668 23. Rezaeiha, A.; Kalkman, I.; Blocken, B. CFD simulation of a vertical axis wind turbine operating at a
669 moderate tip speed ratio: Guidelines for minimum domain size and azimuthal increment. *Renew. Energy*
670 **2017**, *107*, 373–385.

- 671 24. Unsakul, S.; Sranpat, C.; Chaisiriroj, P.; Leephakpreeda, T. CFD-based performance analysis and
672 experimental investigation of design factors of vertical axis wind turbines under low wind speed conditions
673 in Thailand. *J. Flow Control Meas. Vis.* **2017**, *5*, 86–98.
- 674 25. Naccache, G.; Paraschivoiu, M. Development of the dual vertical axis wind turbine using computational
675 fluid dynamics. *J. Fluids Eng.* **2017**, *139*, 121105.
- 676 26. Kao, J.H.; Tseng, P.Y. Application of computational fluid dynamics (CFD) simulation in a vertical axis wind
677 turbine (VAWT) system. *IOP Conf. Ser. Earth Environ.* **2018**, *114*, 012002.
- 678 27. Li, C.; Xiao, Y.; Xu, Y.; Peng, Y.; Hu, G.; Zhu, S. Optimization of blade pitch in H-rotor vertical axis wind
679 turbines through computational fluid dynamics simulations. *Appl. Energy* **2018**, *212*, 1107–1125.
- 680 28. Gokulnath, R.; Devi, P.B.; Senbagan, M.; Manigandan, S. CFD analysis of Savonius type vertical axis wind
681 turbine. *IJMET* **2018**, *9*, 1378–1383.
- 682 29. Elsakka, M.M.; Ingham, D.; Ma, L.; Pourkashanian, M. CFD analysis of the angle of attack for a vertical axis
683 wind turbine blade. *Energy Convers. Manag.* **2019**, *182*, 154–165.
- 684 30. Bachant, P.; Goude, A.; Wosnik, M. Actuator line modelling of vertical-axis turbines. *arXiv* **2018**,
685 arXiv:1605.01449v4.
- 686 31. Burton, T.; Jenkins, N.; Sharpe, D.; Bossanyi, E. *Wind Energy Handbook*, 2nd ed.; Wiley, US, 2011.
- 687 32. Okpue, A.S. Aerodynamic Analysis of Vertical and Horizontal Axis Wind Turbines. Master's Thesis,
688 Michigan State University, East Lansing, MI, USA, 2011.
- 689 33. Shires, A. Development and Evaluation of an Aerodynamic Model for a Novel Vertical Axis Wind Turbine
690 Concept. *Energies* **2013**, *6*, 2501–2520.
- 691 34. Bianchini, A.; Balduzzi, F.; Haack, L.; Bigalli, S.; Müller, B.; Ferrara, G. Development and Validation of a
692 Hybrid Simulation Model for Darrieus Vertical-Axis Wind Turbines. In Proceedings of the ASME Turbo
693 Expo 2019: Turbomachinery Technical Conference and Exposition GT2019-91218, Phoenix, Arizona, USA,
694 17–21 June 2019.
- 695 35. Mikkelsen, R.F. Actuator Disc Methods Applied to Wind Turbines. Ph.D. Thesis, MEK-FM-PHD, No. 2003-
696 02, Technical University of Denmark, Lyngby, Denmark, 2004.
- 697 36. Newman, B.G. Actuator-disc theory for vertical-axis wind turbines. *J. Wind Eng. Ind. Aerodyn.* **1983**, *15*, 347–
698 355.
- 699 37. Linton, D.; Barakos, G.; Widjaja, R.; Thornber, B. A new actuator surface model with improved wake
700 model for CFD simulations of rotorcraft. In Proceeding of the 73rd Annual Forum and Technology Display
701 of the American Helicopter Society, Fort Worth, TX, USA, 9–11 May 2017.
- 702 38. Shen, W.; Zhang, J.; and Sorensen, J. The actuator surface model: A new Navier-Stokes based model for
703 rotor computations. *J. Sol. Energy Eng.* **2009**, *131*, 011002.
- 704 39. Massie, L.; Ouro, P.; Stoesser, T.; Luo, Q. An Actuator Surface Model to Simulate Vertical Axis Turbines.
705 *Energies* **2019**, *12*, 4741.
- 706 40. Bachant, P.; Wosnik, M. Characterising the near-wake of a cross-flow turbine. *J. Turbul.* **2015**, *16*, 392–410.
- 707 41. Riva, L.; Giljarhus, K.E.; Hjertager, B.; Kalvig, S.M. Implementation and application of the actuator line
708 model by OpenFOAM for a vertical axis wind turbine. *IOP Conf. Ser. Mater. Sci. Eng.* **2017**, *276*, 012002.
- 709 42. Sørensen, J.N.; Shen, W.Z. Numerical modelling of wind turbine wakes. *J. Fluids Eng.* **2002**, *124*, 393–399.
- 710 43. Troldborg, N. Actuator Line Modelling of Wind Turbine Wakes. Ph.D. Thesis, Technical University of
711 Denmark, Nils Koppels Allé, Building 403, DK-2800 Lyngby, Denmark, June 2008.
- 712 44. Martinez, L.; Leonardi, S.; Churchfield, M.; Moriarty, P. A comparison of actuator disk and actuator line
713 wind turbine models and best practices for their use. *AIAA J.* **2012**, *16*. doi:10.2514/6.2012-900.
- 714 45. Shamsoddin, S.; Porté-Agel, F. Large Eddy Simulation of vertical axis wind turbine wakes. *Energies* **2014**,
715 *7*, 890–912.
- 716 46. Reynolds, O. On the dynamical theory of incompressible viscous fluids and the determination of the
717 criterion. *Philos. Trans. R. Soc. Lond. A* **1895**, *186*, 123–164.
- 718 47. Hanjalic, K.; Launder, B. A Reynolds stress model of turbulence and its application to thin shear flows. *J.*
719 *Fluid Mech.* **1972**, *52*, 609–638.
- 720 48. Wilcox, D.C. *Turbulence Modelling for CFD*, 2nd ed.; DCW Industries: Inc.: La Canada, CA, USA, 1998.
- 721 49. Wilcox, D.C. Formulation of the k-omega Turbulence Model Revisited. *AIAA J.* **2008**, *46*, 11.
- 722 50. Deardorff, J. A numerical study of three-dimensional turbulent channel flow at large Reynolds numbers. *J.*
723 *Fluid Mech.* **1970**, *41*, 453–480.

- 724 51. Smagorinsky, J. General Circulation Experiments with the Primitive Equation. *Mon. Weather Rev.* **1963**, *91*,
725 99.
- 726 52. Creech, A.C.W. A Three-Dimensional Numerical Model of a Horizontal Axis, Energy Extracting Turbine.
727 Ph.D. Thesis, Heriot-Watt University, Edinburgh, Scotland, UK, March 2009.
- 728 53. Creech, A.; Früh, W.-G.; Clive, P. Actuator volumes and hr-adaptive methods for three-dimensional
729 simulation of wind turbine wakes and performance. *Wind Energy* **2011**, *15*, 847–863.
- 730 54. Creech, A.C.W.; Früh, W.G.; Maguire, A.E. Simulations of an offshore wind farm using large eddy
731 simulation and a torque-controlled actuator disc model. *Surv. Geophys.* **2015**, *36*, 427–481.
- 732 55. Creech, A.; Früh, W.-G. Modelling wind turbine wakes for wind farms. *Alternative Energy and Shale Gas*
733 *Encyclopedia*; Lehr, J., Keeley, J., Eds.; 2016.
- 734 56. Creech, A.C.W.; Borthwick, A.G.L.; Ingram, D. Effects of support structures in an LES actuator line model
735 of a tidal turbine with contra-rotating rotors. *Energies* **2017**, *10*, 726.
- 736 57. McLaren, K.W. Unsteady Loading of High Solidity Vertical Axis Wind Turbines. Ph.D. Thesis, McMaster
737 University, Canada, 2011.
- 738 58. Nobile, R.; Vahdati, M.; Barlow, J.F. Unsteady flow simulation of a vertical axis wind turbine: A two-
739 dimensional study. *Journal of Wind Engineering and Industrial Aerodynamics* **2014**, *125*, 168–179.
- 740 59. Biadgo, A.M. et al. Numerical and analytical investigation of vertical axis wind turbine. *FME Trans.* **2013**,
741 *41*, 49–58.
- 742 60. Bachant, P.; Wosnik, M. Modelling the near-wake of a vertical-axis cross-flow turbine with 2-D and 3-D
743 RANS. *J. Renew. Sustain. Energy* **2016**, *8*, 053311.
- 744 61. Krogstad, P.A.; Eriksen, P.E. Blind test calculations of the performance and wake development for a model
745 wind turbine. *Renew. Energy* **2013**, *50*, 325–333.
- 746 62. Buntine, J.D.; Pullin, D.I. Merger and cancellation of strained vortices. *J. Fluid Mech.* **1989**, *205*, 263–295.
- 747 63. Rezaeiha, A.; Kalkman, I.; Blocken, B. Effect of pitch angle on power performance and aerodynamics of a
748 vertical axis wind turbine. *Appl. Energy* **2017**, *197*, 132–150.
- 749 64. Hwang, I.S.; Lee, Y.H.; Kim, S.J. Optimization of cycloidal water turbine and the performance improvement
750 by individual blade control. *Appl. Energy* **2009**, *86*, 1532–1540.
- 751 65. Zhao, R.; Creech, A.C.W.; Borthwick, A.G.L.; Nishino, T. Coupling of WATTES and OpenFOAM codes for
752 wake modelling behind close-packed contra-rotating vertical-axis tidal rotors. In Proceedings of the 6th
753 Oxford Tidal Energy Workshop, Oxford, UK, 26–27 March 2018.
- 754 66. Schito, P.; Zasso, A. Actuator forces in CFD: RANS and les modelling in OpenFOAM. *J. Phys. Conf. Ser.*
755 **2014**, *524*, 012160.
- 756 67. Jha, P.K.; Churchfield, M.J.; Moriarty, P.J.; Schmitz, S. Guidelines for volume force distributions within
757 actuator line modelling of wind turbines on large-eddy simulation-type grids. *J. Sol. Energy Eng.* **2014**, *136*,
758 031003.
- 759 68. Martínez-Tossas, L.A.; Churchfield, M.J.; Meneveau, C. Optimal smoothing length scale for actuator line
760 models of wind turbine blades. *Wind Energy* **2015**, *20*, 1083–1096.
- 761 69. Tennekes, H.; Lumley, J.L. *A First Course in Turbulence*; the MIT Press: Cambridge, MA, USA, 1972.
- 762 70. LeBlanc, B.P.; Ferreira, C.S. Experimental determination of thrust loading of a 2-bladed vertical axis wind
763 turbine. *J. Phys. Conf. Ser.* **2018**, *1037*, 022043.
- 764 71. Menter, F.R. Two-Equation Eddy-Viscosity Turbulence Models for Engineering Applications. *AIAA J.* **1994**,
765 *32*, 8.
- 766 72. Barthelmie, R.J.; Hansen, K.; Frandsen, S.T.; Rathmann, O.; Schepers, J.G.; Schlez, W.; Phillips, J.; Rados, K.;
767 Zervos, A.; Politis, E.S.; et al. Modelling and measuring flow and wind turbine wakes in large wind farms
768 offshore. *Wind Energy* **2009**, *12*, 431–444.
- 769 73. Bachant, P. Physical and numerical modeling of cross-flow turbines. Ph.D. Thesis, University of New
770 Hampshire, Durham, US, 2016.
- 771 74. Roache, P.J. Perspective: A method for uniform reporting of grid refinement studies. *J Fluid Eng. ASME*
772 **1994**, *116*, 405–413.
- 773 75. Bakhvalov, N.S. Courant–Friedrichs–Lewy condition. In *Encyclopedia of Mathematics*, Hazewinkel Michiel
774 ed.; Springer Science + Business Media, B.V./Kluwer Academic Publishers, Germany, 2001/1994; ISBN 978-
775 1-55608-010-4.

- 776 76. Sheldahl, R.E.; Klimas, P.C. *Aerodynamic Characteristics of Seven Symmetrical Airfoil Sections through 180-*
777 *Degree Angle of Attack for Use in Aerodynamic Analysis of Vertical Axis Wind Turbines*; Energy Report; Sandia
778 National Lab: Albuquerque, NM, USA, 1981.
- 779 77. Ouro, P.; Stoesser, T. An immersed boundary-based large-eddy simulation approach to predict the
780 performance of vertical axis tidal turbines. *Comput. Fluids* **2017**, *152*, 74–87.
- 781 78. Brochier, G.; Fraunie, P.; Beguier, C.; Paraschivoiu, I. Water channel experiments of dynamic stall on
782 Darrieus wind turbine blades. *J. Propuls. Power* **1986**, *2*, 445–449.
- 783 79. Araya, D.B.; Dabiri, J.O. A comparison of wake measurements in motor-driven and flow-driven turbine
784 experiments. *Exp. Fluids* **2015**, *56*, 150.
- 785 80. Ouro, P.; Runge, S.; Luo, Q.; Stoesser, T. Three-dimensionality of the wake recovery behind a vertical axis
786 turbine. *Renew. Energy* **2018**, *133*, 1066–1077.
- 787 81. Piggott, M.; Pain, C.; Gorman, G.; Power, P.; Goddard, A. h, r, and hr adaptivity with applications in
788 numerical ocean modelling. *Ocean Model* **2004**, *10*, 95–113.
- 789 82. Jensen, B.B.B. Numerical study of influence of inlet turbulence parameters on turbulence intensity in the
790 flow domain: Incompressible flow in pipe system. *Proc. IMechE Part E J. Process Mech. Eng.* **2007**, *221*, 177–
791 185.
- 792 83. User Guide: K-Omega Shear Stress Transport (SST)—OpenFOAM. Available online:
793 <https://www.openfoam.com/documentation/guides/latest/doc/guide-turbulence-ras-k-omega-sst.html>
794 (2016-2017).



© 2020 by the authors. Submitted for possible open access publication under the terms and conditions of the Creative Commons Attribution (CC BY) license (<http://creativecommons.org/licenses/by/4.0/>).